Research Square

Preprints are preliminary reports that have not undergone peer review.
They should not be considered conclusive, used to inform clinical practice,
or referenced by the media as validated information.

# Mechanical Integrity and Failure Behavior of Resistance Spot-Welded Dissimilar Joints between Wrought and Additively Manufactured 316L Stainless Steel

**Hong Bo Dinh**
Hanoi University of Science and Technology
**Thi Giang Le**
Thuy Loi University
**Van Thuong Nguyen**
Hanoi University of Science and Technology
**Quang Ngoc Trinh**
Hanoi University of Science and Technology
**Chau Van Tran**
Military Technical Academy: Dai hoc Ky thuat Le Quy Don
**Long Hoang**
Hanoi University of Science and Technology
**Le Duy Han**
Hanoi University of Science and Technology
**Thanh Tuan Nguyen**
tuan.nguyenthanh@hust.edu.vn

Hanoi University of Science and Technology https://orcid.org/0000-0002-5130-8393

**Research Article**

**Keywords:** Selective laser melting, 316L stainless steel, resistance spot welding, dissimilar joining, failure mechanisms

**Posted Date:** November 10th, 2026

**DOI:** https://doi.org/10.21203/rs.3.rs-11471728/v1

**License:** This work is licensed under a Creative Commons Attribution 4.0 International License.
Read Full License

# Mechanical Integrity and Failure Behavior of Resistance Spot-Welded Dissimilar Joints between Wrought and Additively Manufactured 316L Stainless Steel

Hong Bo Dinh[1], Thi Giang Le[2], Van Thuong Nguyen[1], Quang Ngoc Trinh[1,3], Chau Van Tran[4] , Long Hoang[1], Le Duy Han[1,3] Thanh Tuan Nguyen[1]*

[1]School of Mechanical Engineering, Hanoi University of Science and Technology, Hanoi 100000, Vietnam

[2]Faculty of Mechanical Engineering, Thuyloi University, Hanoi 100000, Vietnam

[3]Joining and Welding Research Institute HUST-UOsaka, School of Mechanical Engineering, Hanoi University of Science and Technology, Hanoi 100000, Vietnam

[4]Advanced Technology Center, Le Quy Don Technical University

(E-Mail): tuan.nguyenthanh@hust.edu.vn

**Abstract**

This study investigates nugget formation, microstructural evolution, and failure mechanisms in dissimilar resistance spot welded (RSW) joints between wrought and selective laser melted (SLM) 316L stainless steels. The SLM material exhibits a hierarchical microstructure consisting of melt-pool boundaries, columnar cellular subgrains, and nanoscale cellular networks, in contrast to the equiaxed austenitic structure of the wrought material. Tensile testing reveals pronounced anisotropy in the SLM material between the building and transverse directions. RSW was performed at currents of 5–9 kA using three joint configurations: wrought/wrought, SLM(B)/wrought, and SLM(T)/wrought. The results show that the nugget develops asymmetrically toward the SLM side, while the columnar dendritic region formed during weld-pool solidification exhibits localized chemical heterogeneity, including Ni enrichment along interdendritic boundaries. The SLM side also contains process-induced defects that influence crack initiation and subsequent fracture. At higher welding currents, the dissimilar joints achieve load capacities comparable to the wrought/wrought joints; however, fracture consistently localizes on the SLM side because of the combined effects of lower ductility and process-induced defects. The results demonstrate that the failure behavior of dissimilar RSW joints is governed by the coupled

effects of nugget geometry, weld-solidification microstructure, SLM build orientation, and defect population.

Keywords: Selective laser melting; 316L stainless steel; resistance spot welding; dissimilar joining; failure mechanisms.

## I. Introduction

Laser powder bed fusion (PBF-LB), commonly known as selective laser melting (SLM), has become one of the most widely adopted metal additive manufacturing techniques[1], [2]. The process employs a high-energy laser beam to selectively melt thin, successive layers of metallic powder, enabling the fabrication of highly dense components with intricate geometries that are virtually unattainable through conventional subtractive methods. As a result, advanced structural alloys, particularly austenitic stainless steels such as 316L, nickel-base superalloys including Inconel 625 and 718 have been extensively investigated within the SLM literature, owing to their excellent corrosion resistance, favorable weldability, and broad industrial applicability [3-6]. The rapid solidification inherent to the PBF-LB/SLM process, with cooling rates on the order of $10^6$ K/s [7-8] produces microstructures that differ fundamentally from those of conventionally processed materials [9-11]. Fine cellular substructures, nonequilibrium segregation, and crystallographic texture can increase strength through dislocation-based mechanisms, but they also make the mechanical response sensitive to processing conditions and build orientation. This becomes particularly relevant when an AM component is subjected to a subsequent joining process, because the pre-existing microstructure can influence both heat flow and the response of the material to welding.

The increasing use of AM components in load-bearing structural applications has created an urgent need to understand their joining behavior, particularly their weldability. Several studies have highlighted the challenges inherent to joining AM materials using various fusion welding techniques [12-16]. Elsayed et al. [13] compared the performance of LPBF AISI 316L plates joined via tungsten inert gas (TIG) welding and laser beam welding (LBW). They demonstrated that the high heat input of TIG welding promotes grain coarsening and the formation of coarse dendritic structures consisting of duplex austenite and delta-ferrite phases. In contrast, the

localized energy input and rapid cooling of laser welding produce a narrow fusion zone (FZ) with cellular structures, which significantly enhances micro-indentation hardness. For nickel-base superalloys, Jokisch et al. [14] evaluated the feasibility of laser welding SLM-manufactured IN625 and IN718 tubes, successfully demonstrating joint fabrication without hot cracking. However, they observed that capillary instabilities during keyhole collapse, particularly when laser power is ramped out, consistently lead to pore nests and end-crater cavities in the circular overlap zone. To overcome these limitations, they proposed horizontal beam oscillation and optimized power ramping to improve metal flow and minimize defect formation. Khedr et al. [15] examined the influence of building, inclined, and transverse directions on TIG-welded LPBF 316L joints, establishing that the orientation of columnar grain boundaries relative to the weld path controls thermal dissipation and local cooling rates. When welding is conducted parallel to the build layers, heat transfer is accelerated because conduction proceeds along the columnar boundaries. This rapid heat dissipation refines the dendritic structure, narrows the heat-affected zone (HAZ), increases local dislocation density, and suppresses solidification cracking by retaining a higher delta-ferrite volume fraction, ultimately yielding a joint efficiency of 99.7%. In a related study, Khedr et al. [17] investigated the crystallographic-dependent performance of laser-welded LPBF 316L plates, confirming that the joint configuration parallel to the print layers exhibits the greatest cooling rate, the narrowest FZ width (0.40 mm), and a highly refined grain structure. To characterize these anisotropic behaviors under dissimilar weld joint configurations, Zhang et al. [18] employed digital image correlation to capture full-field surface strain distributions across laser-welded horizontal, vertical, and dissimilar joints. Their findings indicated that strain concentrations and plastic deformations localize exclusively in the fusion zone when the macroscopic load exceeds half the 0.2% proof stress. Owing to microstructural coarsening wherein grain size in the FZ is an order of magnitude larger than in the base metal the weld zone experiences pronounced softening. More recently, Park et al. [16] found that PBF-fabricated 316L stainless steel exhibits unique microstructures (cellular/columnar dendrites), higher dislocation density, and greater surface roughness compared to cold-rolled material in resistance spot welding. These intrinsic characteristics reduce its electrical and thermal conductivity, causing excessive heat generation during resistance spot welding.

Preliminary evidence suggests that SLM 316L stainless steel exhibits distinct weldability characteristics compared with conventional material. Excessive heat generation leads to weld

expulsion at relatively low welding currents, and the achievable nugget diameter in AM 316L under constant current control has been reported to fall below international standards, implying that modified welding parameters may be required. most available studies have considered similar-material joints, such as SLM-to-SLM or wrought-to-wrought combinations. Dissimilar RSW between SLM and wrought 316L has received much less attention, even though this combination is relevant to hybrid manufacturing, where an AM component may need to be attached to a conventionally fabricated structure. The present study therefore examines nugget formation, fusion-zone microstructure, mechanical response, and fracture behavior in dissimilar RSW joints between wrought and SLM 316L. Particular attention is given to the effect of SLM build orientation and welding current, with the aim of relating the observed joint performance to nugget geometry, solidification defects, and the intrinsic mechanical behavior of the two materials.

## 2. Experimental Procedure

### 2.1 Materials and Specimen

The materials used in this study were cold-rolled wrought 316L austenitic stainless steel and SLM 316L stainless steel. The wrought sheet had a nominal thickness of 1.0 mm. The chemical compositions of both materials were measured by optical emission spectroscopy (OES) and are listed in Table 1. The measured Cr and Ni contents were within the ranges specified for 316L stainless steel in ASTM A240. Compared with the wrought material, the SLM 316L contained more Ni (13.532 wt.% versus 10.030 wt.%) and Nb (0.302 wt.% versus 0.004 wt.%). It also contained slightly less C and more N. These compositional differences are relevant when interpreting the mechanical and solidification behavior of the two materials. The SLM material was produced using a commercial powder-bed-fusion system equipped with a 200 W fiber laser and a nominal beam diameter of 115 μm. Powder layers 20 μm thick were deposited and selectively melted using a bidirectional scanning strategy at 500 mm/s, with a hatch spacing of 0.12 mm. The scan strategy included a 67° rotation between successive layers, as illustrated in Fig. 1. The feedstock powder was gas-atomized and approximately spherical, with particle sizes ranging from 10 to 45 μm.

The SLM block used for specimen extraction is shown in Fig. 2a. Two orientations were examined: the building direction (B), in which the specimen axis was parallel to the build direction, and the transverse direction (T), as shown schematically in Fig. 2b. These orientations were selected to capture the anisotropy associated with the SLM microstructure. Wrought and SLM sheets were machined into 60 mm × 20 mm rectangular coupons by electrical discharge machining (EDM). The faying surfaces were ground to 1200 grit SiC paper and then cleaned ultrasonically in acetone for 10 min. All sheets were 1.0 mm thick. For metallographic examination, samples were sectioned from the wrought material and from the SLM material in both orientations, mounted in epoxy, ground with SiC papers from 240 to 4000 grit, and polished using 3 μm and 1 μm diamond suspensions followed by colloidal silica. The microstructures were examined by optical microscopy and SEM (JEOL JSM-8000F) with EDS.

## 2.2 Resistance Spot Welding

RSW was carried out using a pneumatic spot-welding machine fitted with water-cooled CuCrZr electrodes. The electrode tips had a truncated-cone geometry with a tip diameter of approximately 6 mm. A 4 kN electrode force was applied during the squeeze stage to establish stable contact before current was applied. The welding schedule consisted of 20 cycles of squeeze time, 20 cycles of weld time, and 30 cycles of hold time. Heat was generated by electrical resistance at the contact region and produced a localized molten zone that solidified to form the weld nugget. The welding schedule was established from preliminary trials and parameter ranges reported for stainless-steel sheets of similar thickness. Welding current was varied while the other parameters were kept constant. Currents of 5, 6, 7, 8, and 9 kA were investigated. Three joint configurations were prepared: wrought 316L/wrought 316L, SLM 316L(B)/wrought 316L, and SLM 316L(T)/wrought 316L. Two specimens were produced for each welding condition to assess repeatability. The complete welding conditions are summarized in Table 2.

## 2.3 Mechanical test performence

The tensile properties of the base materials were measured in accordance with ASTM E8/E8M. Specimens were machined from the wrought sheet and from the SLM block in the building and transverse orientations, with a thickness of 1 mm. The wrought specimens were prepared with dimensions comparable to those of the SLM specimens. Tests were conducted at

room temperature using a universal testing machine at a crosshead speed of 0.1 mm/min, and engineering stress–strain curves were recorded. The welded joints were evaluated by shear-tension testing using the single-lap configuration shown in Fig. 3. Tests were performed at room temperature with a crosshead speed of 0.1 mm/min. The load–displacement response was recorded for each welding condition. The main quantities considered were the maximum load, the displacement at maximum load, and the resulting failure mode. Failure was classified according to the fracture path as interfacial failure, pull-out failure, or sheet tearing. After testing, the failed specimens were examined macroscopically to identify the fracture location and then by SEM to characterize the fracture morphology and the features associated with crack initiation and propagation.

## 3. Results

3.1 Microstructural characteristics and mechanical properties of wrought of base baterials

The typical microstructure of the wrought 316L austenitic stainless steel used in this study is shown in Fig. 4. The material exhibited a conventional equiaxed grain structure characteristic of austenitic stainless steels in the annealed condition. The grains were generally polygonal in morphology, with annealing twins frequently observed within the grains, a feature typical of low stacking fault energy austenitic stainless steels. No significant second phases or precipitates were observed at the optical microscopy level, consistent with the fully austenitic microstructure expected for 316L stainless steel in the solution-annealed condition.

Figure 5 presents the microstructural characteristics of the SLM 316L along the building direction. The microstructure of the SLM 316L stainless steel exhibited features fundamentally distinct from those of the wrought material, reflecting the non-equilibrium solidification conditions inherent to the laser powder bed fusion process. At low magnification (Figs. 5a and 5b), the characteristic overlapping arc-shaped melt pool boundaries were clearly visible. The melt pools were approximately 50–100 μm wide and 30–50 μm deep, reflecting the successive laser tracks produced during layer-by-layer fabrication. At higher magnification, the material showed a hierarchical cellular structure. Columnar cells approximately 0.5–1 μm wide and several micrometers long extended from the melt-pool boundaries, while much finer cellular networks, about 400–600 nm in diameter, occupied the interior of the melt pools. The arrangement reflects the steep thermal gradients and rapid solidification characteristic of PBF-LB. Rather than a single

uniform grain structure, the SLM material therefore contains features at several length scales, which helps explain its different mechanical response from the wrought steel.

The transverse section showed the scan-track and hatch pattern produced during SLM (Fig. 6). At low magnification, the overlapping laser tracks appeared as parallel bands separated by hatch boundaries. At higher magnification (Fig. 6c), the melt-pool boundaries remained visible and separated regions with different subgrain orientations. Figure 6d, a high-magnification SEM image magnified from Fig. 6c, revealed the interface between columnar cellular and nano-sized cellular subgrain networks along the melt pool boundary. The transition from columnar to equiaxed cellular structures at the melt pool boundary was clearly evident, with the columnar cells growing from the boundary into the melt pool interior and the nano-sized equiaxed cells occupying the central regions of the melt pools. This transition reflects the evolution of the thermal gradient and solidification rate during melt pool solidification, with the highest thermal gradients (and therefore the most directional solidification) occurring at the melt pool boundary where the solidification front initiated.

The engineering stress–strain curves in Fig. 7 show a clear difference between the wrought and SLM materials. The wrought 316L had a yield strength of approximately 250–300 MPa, an ultimate tensile strength of about 580–620 MPa, and elongation above 40%. The SLM material was considerably stronger but less ductile. The transverse orientation reached a yield strength of approximately 550–600 MPa and an ultimate tensile strength close to 700 MPa, whereas the building direction gave approximately 450–500 MPa yield strength and 600–650 MPa ultimate tensile strength. Elongation of the SLM specimens was in the range of 15–25%. The building direction showed slightly greater elongation than the transverse orientation. These results confirm that the SLM material is both stronger and less ductile than the wrought steel, while its tensile response depends on build orientation.

### 3.2 Nugget formation in RSW joints

Figure 8 presents surface macrographs of RSW joints at welding currents of 6 kA, 7 kA, 8 kA, and 9 kA. Figs. 8a–d show the wrought 316L sheet surfaces, while Figs. 8e–h show the SLM 316L (B) sheet surfaces, revealing electrode indentation and thermal oxidation ring evolution. The electrode indentation marks were clearly visible on both sheet surfaces, appearing as circular depressions corresponding to the electrode tip geometry. The indentation depth increased

progressively with welding current, reflecting the higher heat input and corresponding softening of the material at higher currents. At 6 kA, the indentation was relatively shallow, while at 9 kA, the indentation was significantly deeper, with evidence of localized plastic deformation around the indentation perimeter. The thermal oxidation rings colored bands surrounding the electrode indentation exhibited a systematic evolution with welding current. At 6 kA, the oxidation ring was relatively narrow and lightly colored, indicating limited heating of the sheet surface beyond the electrode contact area. At 7 kA and 8 kA, the oxidation ring expanded and exhibited more pronounced coloration, with distinct zones of yellow, brown, and blue corresponding to different oxidation temperatures. At 9 kA, the oxidation ring was extensive, covering a significant portion of the sheet surface around the weld. The SLM 316L surfaces (Figs. 8e–h) exhibited similar oxidation ring evolution to the wrought surfaces, although the coloration patterns were somewhat different, possibly reflecting differences in surface chemistry or oxide stability between the two materials.

Figure 9 presents macrographs showing the nugget geometries of RSW joints between wrought 316L and SLM 316L stainless steels, with the SLM 316L sheet oriented along the building direction. At a welding current of 6 kA (Fig. 9a), the weld nugget exhibited a characteristic lenticular shape with a well-defined fusion zone at the faying interface. The nugget diameter was approximately 3.02 mm, with the fusion zone extending partially through the thickness of both sheets. At a welding current of 9 kA (Fig. 9b), the nugget geometry was significantly larger, with the fusion zone extending nearly through the full thickness of the sheets. The increased heat input at the higher welding current resulted in more extensive melting and a corresponding increase in nugget diameter to approximately 5.78 mm. The characteristic electrode indentation marks were visible on both sheet surfaces, with the indentation depth increasing with welding current due to the higher heat input and corresponding softening of the material.

Figure 10 presents the cross-sectional macrostructure and SEM microstructural features of a dissimilar SLM 316L (T)/wrought 316L resistance spot weld produced at a welding current of 6 kA. The weld nugget was centrally located at the faying interface, with the original sheet interface visible as a horizontal line across the nugget center. The macrograph (Fig. 10a) reveals a pronounced asymmetric nugget profile: the nugget thickness toward the SLM 316L (T) side is significantly greater than that toward the wrought 316L side, indicating asymmetric heat generation and melting across the joint. At higher magnification (Fig. 10b, c), the fusion zone

exhibits a cellular–dendritic solidification structure consisting of primary austenite with interdendritic segregation. The primary dendrite arms are oriented approximately perpendicular to the fusion line, consistent with directional solidification from the cooler base metal toward the nugget center. A high density of dendritic porosity is clearly evident on the SLM 316L (T) side of the nugget, particularly in the central regions where the solidification front converged, which is consistent with shrinkage porosity in the last-solidifying regions. In contrast, no dendritic porosity is observed in the wrought 316L region. In addition, a distinct solidification crack extends through the SLM side of the nugget (Fig. 10b), further highlighting the distinct solidification behavior and greater defect susceptibility of the additively manufactured side compared with the wrought counterpart.

Figure 11 presents more detailed SEM microstructural features of the dissimilar SLM 316L (T) / Wrought 316L resistance spot weld at a welding current of 6 kA. Figures 11b and 11c show SEM micrographs of the left and right fusion line boundaries along the original sheet interface. The fusion line exhibited a clearly defined boundary between the weld nugget and the unmelted base material. On the weld nugget side of the fusion line, the dendritic solidification structure was evident, with primary dendrites growing approximately perpendicular to the fusion line. On the base material side, the original wrought or SLM microstructure was preserved, with no evidence of melting or significant thermal alteration. Figure 11d presents high-magnification SEM views of the central weld nugget highlighting the columnar dendritic solidification and interdendritic porosity. The columnar dendrites exhibited a characteristic oriented growth pattern, with primary dendrite arms extending from the fusion line toward the center of the nugget. The interdendritic regions contained a fine-scale eutectic-like structure resulting from the segregation of alloying elements during solidification. The interdendritic porosity appeared as dark spherical or irregularly shaped features located along the interdendritic boundaries.

To further examine the elemental distribution across the interface between the SLM 316L and wrought 316L sheets, an EDS line scan was conducted across the corona region of the RSW joint, as shown in Fig. 12a. The measured line traverses approximately 100 μm on either side of the sheet interface, with Ni, Cr, and Fe selected as representative alloying elements of 316L stainless steel. The Cr profile remains relatively stable across both sides of the interface, although local fluctuations in signal intensity are observed. The Cr intensity is generally comparable

between the SLM and wrought 316L regions, indicating a relatively similar Cr content in the two materials. Similarly, the Fe signal remains relatively stable away from the interface, with a somewhat lower intensity on the wrought 316L side. On the other hand, The Ni profile shows a relatively clear difference between the two materials. The Ni intensity is generally higher on the SLM 316L side than on the wrought 316L side. This observation is consistent with the chemical compositions presented in Table 2, where the SLM 316L contains approximately 13 wt.% Ni, whereas the wrought 316L contains approximately 10 wt.% Ni. Therefore, the difference in Ni intensity across the interface can be attributed primarily to the inherent compositional difference between the two starting materials. Nevertheless, the Ni profile does not exhibit an abrupt or highly localized peak at the interface, suggesting that there is no pronounced Ni segregation at the SLM/wrought boundary. The EDS maps (Fig. 12b) indicate that the columnar dendritic region on the SLM side of the weld nugget exhibits a chemically heterogeneous solidification structure. The principal alloying elements are generally distributed throughout the matrix, while localized variations in elemental intensity are observed along the interdendritic/intercellular boundaries. In particular, Ni shows a relatively pronounced enrichment along these boundaries, indicating preferential solute redistribution during rapid solidification. This localized chemical heterogeneity reflects the partitioning of alloying elements between the growing dendrites and the remaining liquid during weld-pool solidification and may contribute to the heterogeneous deformation and fracture behavior of the SLM side.

### 3.3 Shear-tension test results

Figure 13 presents the load–displacement responses of the three joint configurations, and Table 2 summarizes the maximum loads and displacements at maximum load. The wrought/wrought joints reached 5.66 ± 0.15 kN at 5 kA. At 6, 7, 8, and 9 kA, their maximum loads were 6.67 ± 0.18, 7.81 ± 0.19, 8.61 ± 0.13, and 8.73 ± 0.15 kN, respectively. The corresponding displacements at maximum load increased from 6.36 ± 0.30 mm at 6 kA to 8.18 ± 0.18, 11.25 ± 0.01, and 12.03 ± 0.08 mm at 7, 8, and 9 kA. Thus, increasing current improved both load capacity and deformation capacity, with the peak load changing relatively little between 8 and 9 kA.

For the SLM(B)/wrought joints (Fig. 13b), the maximum loads at 6, 7, 8, and 9 kA were 5.57 ± 0.14, 7.48 ± 0.16, 8.51 ± 0.19, and 8.73 ± 0.35 kN, respectively. The corresponding displacements at maximum load were 2.39 ± 0.07, 4.81 ± 0.20, 6.53 ± 0.18, and 6.88 ± 0.39 mm.

Although the peak load approached that of the wrought/wrought reference at 8–9 kA, the displacement at maximum load remained substantially lower. For the SLM(T)/wrought joints (Fig. 13c), the maximum loads at 6, 7, 8, and 9 kA were 6.25 ± 0.17, 7.56 ± 0.02, 8.49 ± 0.06, and 8.89 ± 0.28 kN, respectively. The corresponding displacements at maximum load were 2.77 ± 0.07, 5.57 ± 0.08, 6.70 ± 0.21, and 7.40 ± 0.50 mm. The transverse configuration showed greater displacement at maximum load than the building configuration at each common current. Differences in peak load between the two orientations were small at 7–9 kA; these results do not establish a consistent superiority of either orientation in load capacity.

Figure 14a,b compares the maximum loads and displacements at maximum load. At 6 kA, the wrought/wrought reference carried a greater load than either dissimilar configuration. By 8–9 kA, the peak loads of all three configurations were comparable. At 9 kA, the mean peak load of SLM(T)/wrought was slightly higher than those of the other configurations, but the reported spreads overlap. The wrought/wrought joints retained substantially greater displacement at maximum load throughout the common current range. Higher welding current therefore improved the deformation capacity of the dissimilar joints without eliminating the difference from the wrought/wrought reference. Given that two specimens were tested per reported condition, these comparisons are descriptive and do not establish statistical significance.

Figure 14c illustrates the influence of welding current on the fracture energy $W_{max}$ of the three types of RSW specimens. Overall, $W_{max}$ increases progressively with increasing welding current for all three specimen configurations, indicating improved energy absorption and resistance to fracture at higher welding currents. For the wrought 316L/wrought 316L specimens, the fracture energy increases from approximately 15.5 J at 5 kA to 81 J at 9 kA, representing the highest fracture energy over the entire investigated current range. In comparison, the two hybrid joints exhibit substantially lower fracture energies. The 316L SLM (B) + wrought 316L specimens show an increase from approximately 9 J at 6 kA to 44 J at 9 kA, while the 316L SLM (T) + wrought 316L specimens increase from approximately 11 J to 48 J over the same current range. At 6 kA, both hybrid joints exhibit considerably lower $W_{max}$ than the wrought 316L/wrought 316L joint; however, the difference becomes progressively smaller with increasing welding current. Between the two SLM orientations, the SLM (T) configuration generally exhibits slightly higher fracture energy than the SLM (B) configuration, particularly at 7–9 kA. The overall increase in fracture energy with welding current can be attributed to the greater heat input associated with

higher current, which promotes the formation of a larger and more developed weld nugget and consequently increases the load-bearing area and deformation capacity of the joint. Nevertheless, the consistently higher $W_{max}$ of the wrought/wrought joints indicates that the hybrid joints retain a lower fracture-energy capacity, with the difference becoming less pronounced at higher welding currents.

### 3.4 Failure modes and fracture analysis

Figure 15 presents post-shear-tension macrographs of dissimilar SLM 316L (T)/Wrought 316L joints welded at 7 kA, 8 kA, and 9 kA, showing both top-down fracture appearances (left) and side-profile views (right). A clear and systematic evolution in fracture behavior was observed with increasing welding current, reflecting the progressive improvement in nugget quality and load-transfer capability. At 7 kA (Fig. 15a), the joint exhibited a mixed failure mode, characterized by partial pull-out of the weld nugget from one sheet combined with partial interfacial fracture along the fusion zone. The top-down view revealed a fractured surface with distinct regions: some areas displayed ductile tearing features indicative of pull-out failure, while other areas showed relatively flat fracture surfaces characteristic of interfacial failure. The side-profile view provided further insight into the fracture path, showing that failure initiated at the periphery of the nugget and propagated through two competing routes, partially through the nugget itself and partially along the interface between the nugget and the base material. This mixed mode suggests that at 7 kA, the nugget had not yet reached the critical size or strength required to fully resist crack propagation, resulting in a competition between interfacial debonding and nugget extraction. When the welding current was increased to 8 kA (Fig. 15b), the failure mode shifted predominantly to pull-out. The top-down view showed a circular fracture surface corresponding to the nugget perimeter, with evidence of ductile tearing around the entire circumference. The side-profile view clearly revealed the nugget protruding from the surface of one sheet, confirming that pull-out was the dominant failure mechanism. Some localized interfacial failure was still observable, but this was limited to small regions and did not compromise the overall pull-out behavior. This transition indicates that the nugget had grown sufficiently to resist interfacial crack propagation, forcing the fracture path to deviate through the surrounding base material. At 9 kA (Fig. 15c), the failure mode became exclusively pull-out, with the weld nugget cleanly extracted from one sheet. The top-down view displayed a complete circular fracture surface with ductile tearing uniformly distributed

around the entire circumference. The side-profile view showed the nugget fully pulled out, exhibiting the characteristic button morphology typical of strong RSW joints. The complete absence of interfacial failure at this current confirms that the nugget strength and integrity were sufficient to exceed the load-carrying capacity of the surrounding base material, resulting in the most favorable failure mode from a structural integrity perspective.

A comparison of failure modes between similar and dissimilar joints at 9 kA is presented in Fig. 16. The wrought/wrought joint (Fig. 16a) exhibited a classic pull-out failure mode, with the weld nugget being pulled out cleanly from one of the sheets. The top-down view showed a complete circular fracture surface with ductile tearing around the entire circumference. The side-profile view revealed that failure occurred through the base material immediately adjacent to the nugget, leaving the nugget intact and protruding from the opposite sheet. This failure mode is characteristic of strong RSW joints where the nugget strength exceeds the strength of the surrounding base material, and it is generally considered desirable because it ensures that fracture occurs through the base metal rather than through the weld itself. The SLM(B)/wrought joint (Fig. 16b) also exhibited a pull-out failure mode, though with some notable differences in fracture characteristics. The top-down view showed a circular fracture surface, but the surface appeared somewhat rougher than that of the wrought/wrought joint. More significantly, the side-profile view revealed that failure occurred preferentially on the SLM side of the joint, with the nugget being pulled out of the SLM sheet rather than the wrought sheet.

Figure 17 presents the fracture surface morphology of the resistance spot weld produced at 6 kA after tensile-shear testing, which exhibited a pull-out fracture mode. The macroscopic overview (Fig. 17a) shows an intact, cylindrical weld button that has been completely torn from the wrought 316L sheet while remaining attached to the SLM 316L substrate.Detailed fractographic examination of the pulled-out button reveals a characteristic dendritic solidification structure. The peripheral region (Fig. 17b) exhibits pronounced surface steps, plastic shearing, and longitudinal solidification cracks aligned parallel to the solidification direction. Such pre-existing cracks act as stress concentrations and can significantly reduce the energy required for crack initiation during tensile-shear deformation. At higher magnification (Fig. 17c, d), the fracture surface is dominated by primary and secondary dendritic arms along with solidification shrinkage. The primary dendritic arms are oriented along the direction of heat flow, while the secondary arms grow perpendicular to the primary arms, reflecting the cellular-dendritic solidification mode of the

fusion zone. The presence of solidification shrinkage indicates that the last-solidifying regions could not be adequately fed, resulting in microvoids and interdendritic cavities. The fracture path followed interdendritic regions and shrinkage defects, indicating that the solidification structure and the associated defects played an important role in damage initiation and crack propagation.

## 4. Discussion

### 4.1 Nugget formation and solidification in dissimilar RSW joints

One of the most notable observations in this study is the asymmetric growth of the weld nugget in dissimilar joints, particularly at low welding currents. When joining SLM and wrought 316L, the melt pool and resulting nugget consistently shifted toward the SLM side. This asymmetry is clearly evident in Figs. 9–11, where the nugget appears larger, both wider and deeper, on the SLM side compared to the wrought side. This behavior can be attributed to differences in electrical and thermal properties between the two materials [16], [19]. The SLM 316L, with its fine cellular-dendritic structure and higher density of grain boundaries (Figs. 5 and 6), exhibits higher electrical resistivity than its wrought counterpart. According to Joule's law, heat generation during RSW is proportional to the electrical resistance at the faying interface; therefore, the SLM side generates more heat for a given welding current. Additionally, the thermal conductivity of SLM 316L is somewhat lower than that of the wrought material due to the presence of numerous grain boundaries and dislocations that scatter phonons. This reduced thermal conductivity means that heat generated on the SLM side is dissipated less efficiently into the surrounding material, further promoting localized heating and more extensive melting. The combination of higher heat generation and lower heat dissipation creates a thermal imbalance that favors nugget growth toward the SLM material [20].

The larger molten region on the SLM side was accompanied by a greater concentration of solidification defects. Cross-sectional observations showed more interdendritic porosity and local solidification cracking on the SLM side than on the wrought side. A larger molten volume undergoes greater total contraction during solidification, and the last-solidifying regions may not receive sufficient liquid feeding to compensate for this shrinkage. The columnar dendritic network can further restrict liquid flow between growing dendrites. The resulting defect distribution is

therefore asymmetric: the SLM side experiences more extensive melting, but the solidified region is also more susceptible to shrinkage-related defects [21].

Expulsion was also observed at lower welding currents in the dissimilar joints than in the wrought/wrought joints. One plausible contribution is the surface condition of the SLM material. As-built SLM surfaces are generally rougher than rolled sheet, so the real contact area at the faying interface is distributed among numerous asperities. These local contacts can produce concentrated electrical heating and an earlier rise in interface temperature [22], [23]. Under marginal heat-input conditions, such local heating can destabilize the molten zone and promote expulsion before a well-developed nugget is established . The different oxidation patterns visible in Fig. 8 are also consistent with differences in surface condition and thermal exposure.

The solidification morphology provides further evidence of the thermal conditions during RSW. Primary dendrites grew approximately normal to the fusion line, indicating that solidification proceeded along the dominant temperature gradients established by heat extraction into the surrounding base metal and the water-cooled electrodes. As solidification progressed, solute-enriched liquid was confined to increasingly narrow interdendritic channels. Consequently, interdendritic porosity was concentrated in the last-solidifying regions, where liquid feeding was least effective, and was more pronounced on the SLM side. Similar welding studies associate columnar growth normal to the fusion boundary with the direction of maximum thermal gradient, while shrinkage porosity is linked to inadequate feeding during the final stages of solidification [24]. The fusion-boundary morphology also differed between the two materials. On the wrought side, the relatively sharp transition from equiaxed base metal to columnar dendrites indicates a distinct fusion boundary and direct directional growth into the molten nugget. In contrast, the pre-existing cellular or columnar-cellular structure of the SLM material created a different nucleation and growth environment. SLM alloys commonly retain fine cellular substructures generated by rapid solidification, and these structures can persist within larger columnar grains or influence epitaxial growth during subsequent thermal processing. The resulting transition from the SLM base metal to the weld dendrites was therefore more gradual, with the inherited cellular structure affecting dendrite orientation, spacing, and liquid-feeding paths. These differences help explain the asymmetric nugget profile and the greater concentration of shrinkage-related defects on the SLM side [25].

These findings highlight an important practical consideration for the RSW of dissimilar joints involving SLM materials. Unlike welding similar wrought/wrought joints, where process parameters can be optimized based on well-established guidelines, dissimilar joints require a more nuanced approach. The asymmetric nugget growth, the increased susceptibility to porosity on the SLM side, and the tendency for premature expulsion all need to be taken into account when selecting welding parameters. Simply applying the same welding schedule used for wrought/wrought joints is unlikely to produce optimal results. Instead, process optimization must balance the competing demands of achieving sufficient nugget size on both sides of the joint while minimizing defects and avoiding expulsion. This may require adjustments to welding current, electrode force, or welding time to account for the distinct thermal and electrical behavior of the SLM material. The results of this study suggest that using a slightly higher welding current than that typically used for wrought/wrought joints can be beneficial for dissimilar joints, as it promotes more complete fusion on the wrought side while still achieving acceptable nugget quality on the SLM side provided that the current is not so high as to cause excessive expulsion.

### 4.2 Mechanical performance of dissimilar RSW joints

The shear-tension results show that the difference between dissimilar and wrought/wrought joints is most apparent at lower welding currents. At 5–6 kA, the dissimilar joints had smaller effective load-transfer regions and were more affected by defects on the SLM side. Because the nugget grew preferentially toward the SLM material, the fusion region on the wrought side could remain comparatively underdeveloped. This limits the effective area available for load transfer and leaves the defect-rich SLM side more exposed to the applied stress. These effects together account for the lower peak loads measured at the lower currents. Once the current reached 7 kA and above, the peak loads of the dissimilar joints moved closer to the wrought/wrought reference. Additional heat promoted nugget growth on the wrought side and produced a more continuous fusion zone. The difference between the two SLM orientations was also relatively modest in peak load, although the T-oriented joints generally showed comparable or slightly higher values at the higher currents. This behavior reflects the orientation-dependent response of the SLM base material rather than a simple effect of nugget size alone.

The displacement at maximum load reveals a more persistent difference between the joint configurations. The wrought/wrought joints reached $6.36 \pm 0.30$ mm at 6 kA and $12.03 \pm 0.08$ mm

at 9 kA, whereas the SLM(B)/wrought joints ranged from 2.39 ± 0.07 to 6.88 ± 0.39 mm and the SLM(T)/wrought joints from 2.77 ± 0.07 to 7.40 ± 0.50 mm. Thus, even when the peak loads became similar, the joints containing SLM 316L still accommodated substantially less deformation. This difference is consistent with the base-material tensile results: SLM 316L has higher strength but considerably lower elongation than the wrought steel. During lap-shear loading, the more ductile wrought sheet can accommodate substantial plastic deformation, whereas the SLM side reaches its damage tolerance earlier.

The repeated occurrence of fracture on the SLM side supports this interpretation. The cellular/dendritic microstructure, together with interdendritic porosity and solidification defects, provides preferential sites for local strain concentration and damage initiation. Once a crack forms, these defects can facilitate its propagation through the defect-rich SLM-side region. Thus, the fracture location reflects not only the weld geometry but also the intrinsic deformation behavior of the additively manufactured material. Increasing the welding current improves nugget development and increases the overall displacement to failure, but it does not eliminate the underlying ductility difference between the SLM and wrought materials. The slightly different displacement responses of the B- and T-oriented joints further indicate that build orientation remains mechanically relevant after welding. Powder-bed-fusion materials can retain orientation-dependent properties because their layer structure, grain morphology, texture, and defect distribution vary with the build direction [26]. At 5–6 kA, the smaller nugget and the greater influence of porosity and solidification defects make crack initiation easier and limit both load and displacement. At 7–8 kA, better nugget development shifts the dominant failure mode toward pull-out and allows greater deformation, although fracture still occurs on the SLM side. At 9 kA, the peak loads approach those of the wrought/wrought joints, but the displacement remains lower. In other words, increasing the welding current can substantially improve load transfer, but it cannot fully compensate for the lower deformation capacity of the SLM material.

The comparison between SLM(B)/wrought and SLM(T)/wrought joints further demonstrates the influence of build orientation. At higher welding currents, the B-oriented configuration generally supported slightly greater loads, whereas the T-oriented joints exhibited slightly greater displacement at maximum load. These differences are consistent with the anisotropic tensile response of the SLM material and indicate that the orientation of the cellular/dendritic structure, melt-pool boundaries, and associated defects relative to the applied

load affects both load-bearing capacity and damage development. From a process perspective, the results indicate a relatively narrow balance between nugget development and defect formation. Insufficient heat input leaves the wrought side under-fused and limits load transfer, whereas excessive or highly localized heating promotes expulsion and solidification defects on the SLM side. In the present experiments, increasing the current toward 8–9 kA improved the mechanical response and promoted pull-out-type failure, indicating more effective nugget formation. However, further increases should not be assumed to be beneficial because expulsion can introduce shrinkage voids, solidification cracks, and other discontinuities within the nugget [27]. Further optimization should consider welding current together with electrode force, weld time, and the condition of the SLM faying surface rather than adjusting current alone.

### 4.3 Implications for engineering applications

The results indicate that dissimilar RSW can provide load capacities close to those of wrought/wrought 316L joints when the welding current is sufficiently high. At 8–9 kA, the difference in peak load became relatively small, showing that an appropriately developed nugget can transfer substantial load even though one side of the joint is additively manufactured. This is relevant to hybrid structures in which SLM and conventionally fabricated components must be joined. At the same time, similar peak load does not mean similar overall mechanical behavior. The lower displacement and fracture energy of the SLM-containing joints show that their ability to accommodate plastic deformation remains more limited.

Build orientation should be considered during component and joint design. The tensile results show that the SLM material is anisotropic, and that some of this orientation dependence remains after welding. Melt-pool boundaries, cellular or columnar structures, and defect populations can be oriented differently relative to the applied load, affecting both strength and crack development. Studies of SLM 316L similarly report orientation-dependent tensile and fatigue behavior, with build direction influencing microstructure, defect alignment, and crack propagation [28]. Where the service-loading direction is known, the orientation of the printed structure should therefore be selected together with the component geometry and weld location. In practice, this choice is constrained by printability, support requirements, part geometry, and manufacturing time. Build orientation is consequently an engineering compromise between production efficiency and the mechanical response required after welding. The consistent fracture

location on the SLM side is also useful for quality control. The SLM-side fusion-zone region should receive particular attention during weld assessment because interdendritic porosity and solidification cracks can act as local stress concentrators. This concern is especially relevant under fatigue or severe service loading, where defects that are tolerable in a tensile-shear test may promote early crack initiation. Defect size, shape, and orientation are known to influence the fatigue behavior of SLM 316L [29] . The strong dependence on welding current, especially at 5–6 kA, further shows that a conventional wrought/wrought welding schedule should not be transferred directly to the dissimilar configuration. Within the range studied here, currents of 8–9 kA produced better nugget development and higher load and displacement than the lower-current conditions. These values should be treated as an experimental process window, not as a universal optimum, because the appropriate current depends on sheet thickness, electrode geometry, force, weld time, surface condition, and machine characteristics. Welding current should therefore be optimized together with electrode force and weld time. Increasing current may enlarge the nugget, but excessive heat input can promote expulsion and introduce shrinkage voids or solidification cracks. Pulsed or ramped schedules may be useful future approaches because they could improve heat-input control and help distinguish surface-condition effects from the intrinsic response of the SLM microstructure.

The earlier occurrence of expulsion in the dissimilar joints also suggests that surface preparation deserves attention. Roughness on an as-built SLM surface can increase local contact resistance and concentrate heating at the faying interface. Grinding or machining the faying surface may reduce this variability and provide a more stable contact condition. Pulse schedules or other controlled heat-input strategies could also be investigated in future work to separate the effects of surface condition from those of the intrinsic SLM microstructure. Interdendritic porosity is another issue that should be considered when the joints are intended for demanding service. The present tensile-shear tests show that the joints can still carry substantial loads at higher currents, but the observed porosity and solidification cracking provide obvious sites for local damage initiation. Their influence may become more important under fatigue or corrosive service, although those conditions were not examined in the present study. Future work should therefore assess the role of weld-induced defects under cyclic loading and in representative service environments.

Nugget size remains a useful qualification parameter, but the present results also show that diameter alone does not fully describe joint quality. A joint may have a sufficiently large nugget

while still containing porosity or solidification cracks that affect deformation and fracture. The numerical comparison with AWS [30] and ISO [31] nugget-size criteria should be checked against the exact sheet thickness and the applicable edition of each standard before publication; the specimens used here were 1.0 mm thick. For this reason, nugget diameter should be considered together with failure mode, defect population, and mechanical response when assessing dissimilar SLM/wrought spot welds.

## 5. Conclusions

This study investigated the nugget formation, microstructural evolution, mechanical response, and failure behavior of resistance spot welded dissimilar joints between wrought and SLM 316L stainless steels, with particular emphasis on the effects of welding current and SLM build orientation. The main conclusions are as follows:

- The two base materials had distinctly different microstructures and mechanical responses. Wrought 316L showed an equiaxed austenitic grain structure, whereas SLM 316L contained overlapping melt-pool boundaries, columnar cellular features, and fine cellular networks. The SLM material was stronger but less ductile, and its tensile properties depended on build orientation.
- Welding current strongly affected nugget development and joint performance. Increasing the current from 6 to 9 kA generally increased the nugget size, peak load, displacement at maximum load, and fracture energy. The effect was particularly important at the lower currents, where incomplete nugget development and welding-induced defects limited load transfer.
- The dissimilar joints developed asymmetric fusion zones, with more extensive melting toward the SLM side. The fusion zone contained cellular–dendritic solidification structures, and interdendritic porosity together with local solidification cracking was concentrated on the SLM side. The observed defect distribution is consistent with the larger molten volume and the solidification conditions in this region.
- Expulsion occurred at lower welding currents in the dissimilar joints than in the wrought/wrought reference. The surface condition of the SLM material is a likely contributor because local asperities can increase contact resistance and concentrate heating at the faying interface.

- The maximum load and displacement at maximum load increased with welding current for all joint configurations. At higher currents, both SLM/wrought configurations approached the load capacity of the wrought/wrought reference. Although the difference in peak load became smaller at higher current, the SLM/wrought joints continued to show lower displacement and fracture energy than the wrought/wrought joints. Increasing nugget size can improve load transfer, but it does not remove the lower deformation capacity associated with the SLM material.
- Fracture consistently occurred on the SLM side of the dissimilar joints. The result emphasizes that joint performance is controlled not only by nugget size and welding conditions, but also by the microstructure, defect population, and build orientation of the additively manufactured material. These factors should therefore be considered together when designing RSW joints that combine SLM 316L with conventionally fabricated components.

## References

[1] Chowdhury, S., Yadaiah, N., Prakash, C., Ramakrishna, S., Dixit, S., Gupta, L. R., & Buddhi, D., Laser powder bed fusion: a state-of-the-art review of the technology, materials, properties & defects, and numerical modelling, Journal of Materials Research and Technology 20 (2022) 2109-2172.

[2] Oliveira, J. P., LaLonde, A. D., & Ma, J., Processing parameters in laser powder bed fusion metal additive manufacturing, Materials & Design 193 (2020) 108762.

[3] Tang, C., Zhao, J., Wang, Z., Zhao, Y., Wang, T., Experimental investigation on the effect of process parameters in additive/subtractive hybrid manufacturing 316L stainless steel, The International Journal of Advanced Manufacturing Technology 121 (2022) 2461-2481.

[4] Moussaoui, K., Rubio, W., Mousseigne, M., Sultan, T., & Rezai, F. J. M. S., Effects of Selective Laser Melting additive manufacturing parameters of Inconel 718 on porosity, microstructure and mechanical properties, Materials Science and Engineering: A 735 (2018) 182-190.

[5] Amato, K. N., Gaytan, S. M., Murr, L. E., Martinez, E., Shindo, P. W., Hernandez, J., Medina, F. J. A. M., Microstructures and mechanical behavior of Inconel 718 fabricated by selective laser melting, Acta Materialia 60 (2012) 2229-2239.

[6] Leary, M., Mazur, M., Williams, H., Yang, E., Alghamdi, A., Lozanovski, B., Brandt, M., Inconel 625 lattice structures manufactured by selective laser melting (SLM): Mechanical properties, deformation and failure modes, Materials & Design 157 (2018) 179-199.

[7] Farshidianfar, M. H., Khajepour, A., & Gerlich, A. P., Effect of real-time cooling rate on microstructure in laser additive manufacturing, Journal of Materials Processing Technology 231 (2016) 468-478.

[8] Bertoli, U. S., Guss, G., Wu, S., Matthews, M. J., & Schoenung, J. M., In-situ characterization of laser-powder interaction and cooling rates through high-speed imaging of powder bed fusion additive manufacturing, Materials & Design 135 (2017) 385-396.

[9] Zhao, C., Bai, Y., Zhang, Y., Wang, X., Xue, J. M., & Wang, H., Influence of scanning strategy and building direction on microstructure and corrosion behaviour of selective laser melted 316L stainless steel, Materials & Design 209 (2021) 109999.

[10] Dixit, S., Liu, S., Murdoch, H. A., & Smith, P. M., Investigating build orientation-induced mechanical anisotropy in additive manufacturing 316L stainless steel, Materials Science and Engineering: A 880 (2023) 145308.

[11] Leicht, A., Yu, C. H., Luzin, V., Klement, U., & Hryha, E., Effect of scan rotation on the microstructure development and mechanical properties of 316L parts produced by laser powder bed fusion, Materials Characterization 163 (2020) 110309.

[12] Fri, K., Laazizi, A., Bensada, M., Alami, M. E., Ouannou, A., Akhrif, I., Fajoui, J. Microstructural and heat treatment analysis of 316L elaborated by SLM additive manufacturing process, The International Journal of Advanced Manufacturing Technology, 124 (2023) 2289-2297.

[13] Elsayed, M., Khedr, M., Järvenpää, A., Gaafer, A. M., & Hamada, A., Microstructure and hardness properties of additively manufactured AISI 316L welded by tungsten inert gas and laser welding techniques, Materials 17 (2024) 4489.

[14] Jokisch, T., Marko, A., Gook, S., Üstündag, Ö., Gumenyuk, A., & Rethmeier, M., Laser welding of SLM-manufactured tubes made of IN625 and IN718, Materials 12 (2019) 2967.

[15] Khedr, M., Abdelghany, A. W., Elsayed, M., Gaafer, A. M., Järvenpää, A., & Hamada, A., Laser welding of additively manufactured 316L stainless steel fabricated with different building orientations, Welding in the World (2026) 1-24.

[16] Park, S., Kim, S., Seo, S., Yu, J., & Park, J., Thermal Behavior and Weldability of Resistance Spot Welded Stainless Steel 316L: Comparative Impact of Additive Manufacturing and Cold Rolling, Metals and Materials International 32 (2026) 353-371.

[17] Khedr, M., Elsayed, M., Jaskari, M., Abdel-Aleem, H. A., Gaafer, A. M., & Hamada, A., Effect of building orientation on weld characteristics of additively manufactured 316L stainless steel: Microstructure and mechanical properties, Materials Science and Engineering: A 913 (2024) 147086.

[18] Zhang, R., Buchanan, C., Matilainen, V. P., Daskalaki-Mountanou, D., Britton, T. B., Piili, H., & Gardner, L., Mechanical properties and microstructure of additively manufactured stainless steel with laser welded joints, Materials & Design 208 (2021) 109921.

[19] Li, Y., & Gu, D., Parametric analysis of thermal behavior during selective laser melting additive manufacturing of aluminum alloy powder, Materials & Design 63 (2014) 856-867.

[20] Simmons, J. C., Chen, X., Azizi, A., Daeumer, M. A., Zavalij, P. Y., Zhou, G., & Schiffres, S. N., Influence of processing and microstructure on the local and bulk thermal conductivity of selective laser melted 316L stainless steel, Additive Manufacturing 32 (2020) 100996.

[21] Olakanmi, E. O., Cochrane, R. F., & Dalgarno, K. W., A review on selective laser sintering/melting (SLS/SLM) of aluminium alloy powders: Processing, microstructure, and properties, Progress in Materials Science 74 (2015) 401-477.

[22] Hwang, I. S., Kang, M. J., & Kim, D. C., Expulsion reduction in resistance spot welding by controlling of welding current waveform, Procedia Engineering 10 (2011) 2775-2781.

[23] Liang, J., Zhang, H., Qiu, X., & Shi, Y., Characteristics of the resistance spot welding joints in dissimilar thickness dual-phase steels, ISIJ International 55 (2015) 2002-2007.

[24] Xu, H., Zhao, M., Wang, R., Han, L., Cheng, X., & Fang, Y., The Role of Element Segregation in the Fracture Mechanism and Performance of Spot-Welded AlSi7MnMg Aluminum Alloy Joints, Materials 19 (2026) 747.

[25] Qiu, C., Kindi, M. A., Aladawi, A. S., & Hatmi, I. A., A comprehensive study on microstructure and tensile behaviour of a selectively laser melted stainless steel, Scientific Reports 8 (2018) 7785.

[26] Aiza, I., Baldi, C., De La Vega, F. M., Sebastiani, S., Veronese, N. E., Yousefi, M., Bagherifard, S., Effects of build orientation and inclined features on physical, microstructural and mechanical properties of powder bed fusion additively manufactured metallic parts, Progress in Materials Science 147 (2025) 101357.

[27] Wan, X., Wang, Y., & Zhang, P., Effects of welding schedules on resistance spot welding of DP600 steel, ISIJ International 54 (2014) 2375-2379.

[28] Yankin, A., Perveen, A., & Talamona, D., Investigation and prediction of fatigue performance of SLM 316 L stainless steel based on small build orientation variations and heat treatment effects, Scientific Reports 15 (2025) 4583.

[29] Avanzini, A., Fatigue behavior of additively manufactured stainless steel 316L, Materials 16 (2022) 65.

[30] AWS D8.1M:2021, Specification for Automotive Weld Quality – Resistance Spot Welding of Steel, American Welding Society (2021).

[31] ISO 14373:2015, Resistance Welding — Procedure for Spot Welding of Uncoated and Coated Low Carbon Steels, International Organization for Standardization, Geneva (2015).

## Declarations

### Funding

This research was funded by the Vietnam National Foundation for Science and Technology Development (NAFOSTED) under research grant No. 107.02-2025.63.

### Conflicts of Interest/Competing Interests

The authors declare that they have no known competing financial interests or personal relationships that could have appeared to influence the work reported in this paper.

### Data Availability

The data generated and analyzed during the current study are available from the corresponding author upon reasonable request.

## List of tables and figures

Table 1. Chemical composition of wrought 316L and SLM 316L stainless steels measured by OES (wt.%)

| Element | C | Si | Mn | S | P | Cr | Ni | Al |
|---|---|---|---|---|---|---|---|---|
| Wrought 316L | 0.0210 | 0.367 | 1.470 | 0.0072 | 0.0382 | 17.009 | 10.030 | 0.0014 |
| SLM 316L | 0.0168 | 0.60 | 0.892 | 0.0112 | 0.0132 | 17.682 | 13.532 | 0.0045 |
| Element | Cu | Nb | Ti | W | Pb | N | Fe | - |
| Wrought 316L | 0.0483 | 0.004 | 0.0055 | 0.0073 | 0.0030 | 0.0814 | 68.385 | - |
| SLM 316L | 0.3064 | 0.302 | 0.0280 | 0.0459 | 0.0036 | 0.1436 | 64.166 | - |

Table 2. Summary of shear-tension test results for wrought/wrought, SLM(B)/wrought, and SLM(T)/wrought RSW joints at different welding currents.

| Welding current (kA) | Wrought-wrought specimen | | Wrough-SLM(B) specimen | | Wrough-SLM(T) specimen | |
|---|---|---|---|---|---|---|
| | Maximum Load (kN) | Displacement at Maximum Load (mm) | Maximum Load (kN) | Displacement at Maximum Load (mm) | Maximum Load (kN) | Displacement at Maximum Load (mm) |
| 5 | 5.66 ± 0.15 | 3.62 ± 0.15 | - | - | - | - |
| 6 | 6.67 ± 0.18 | 6.36 ± 0.30 | 5.57 ± 0.14 | 2.39 ± 0.07 | 6.25 ± 0.17 | 2.77 ± 0.07 |
| 7 | 7.81 ± 0.19 | 8.18 ± 0.18 | 7.48 ± 0.16 | 4.81 ± 0.20 | 7.56 ± 0.02 | 5.57 ± 0.08 |
| 8 | 8.61 ± 0.13 | 11.25 ± 0.01 | 8.51 ± 0.19 | 6.53 ± 0.18 | 8.49 ± 0.06 | 6.70 ± 0.21 |
| 9 | 8.73 ± 0.15 | 12.03 ± 0.08 | 8.73 ± 0.35 | 6.88 ± 0.39 | 8.89 ± 0. 28 | 7.40 ± 0.50 |

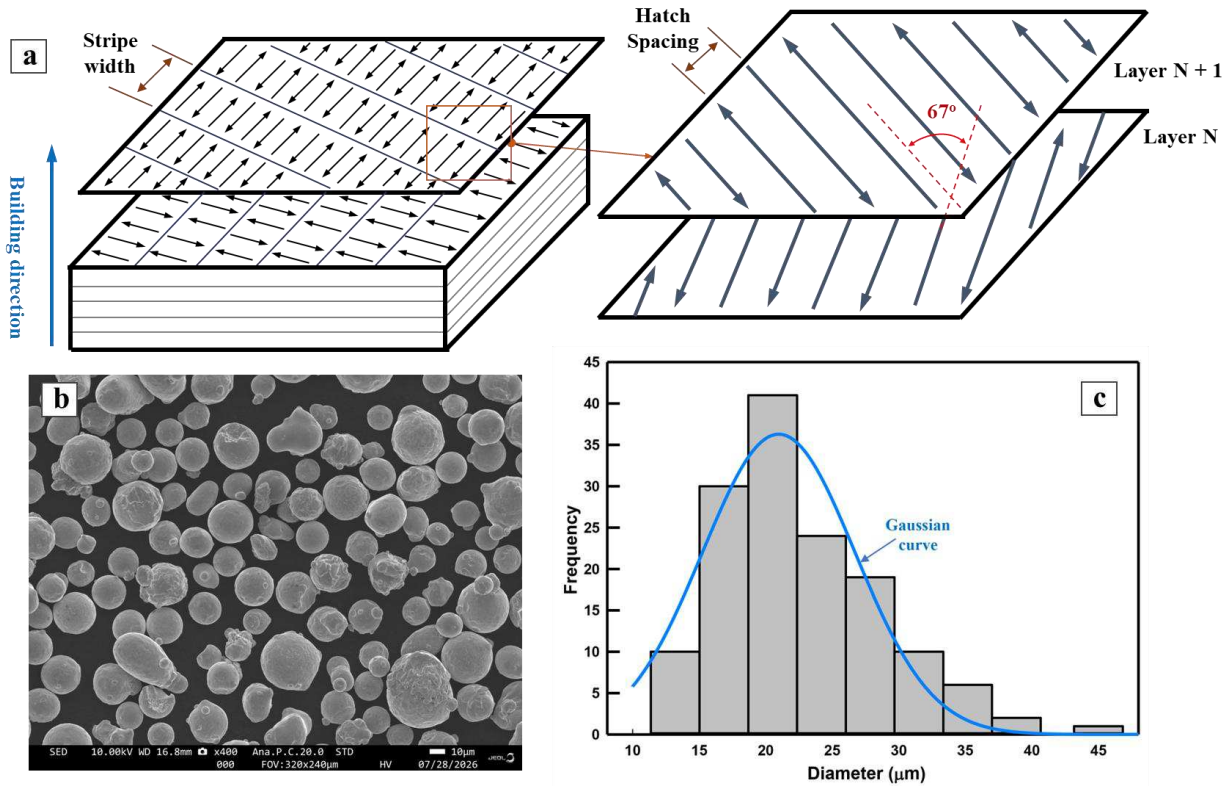



Figure 1. Schematic representation of laser scanning strategies in metal additive manufacturing: (left) stripe scanning strategy showing the stripe width and bidirectional laser paths along the building direction; (right) inter-layer scanning strategy illustrating hatch spacing and a 67° rotation angle between successive layers (Layer $N$ and Layer $N + 1$), (b) SEM micrograph showing the spherical morphology and size distribution of the metallic powder feedstock, (c) (c) Particle size distribution histogram of the powder fitted with a Gaussian curve, indicating particle diameters ranging predominantly between 10 μm and 45 μm.

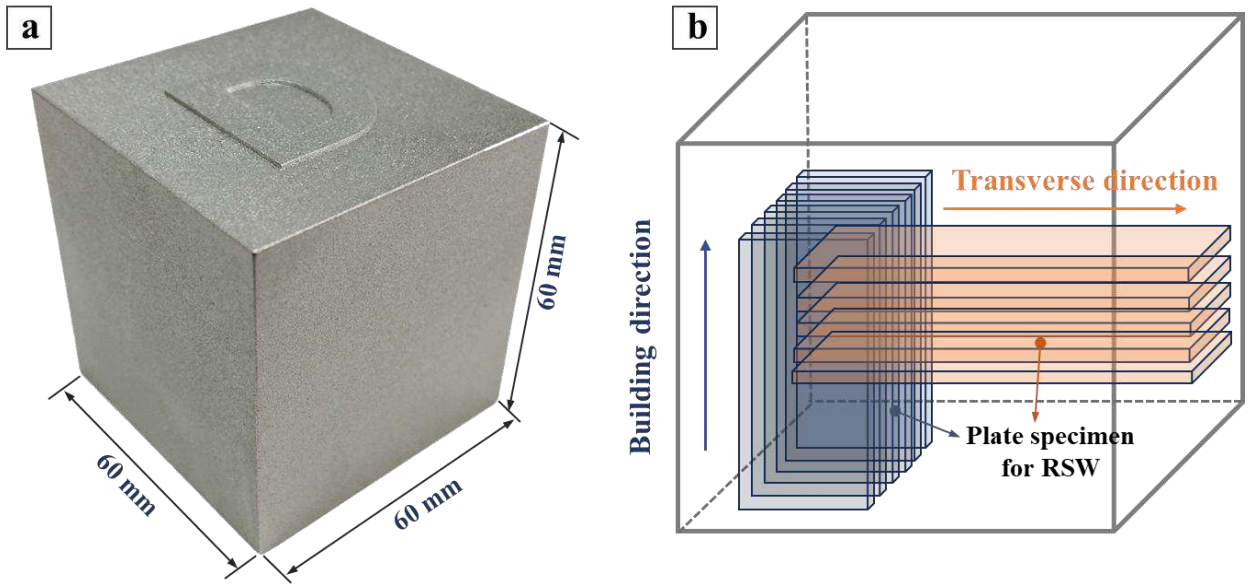



Figure 2. (a) Photograph of the additively manufactured cubic block, (b) Schematic diagram illustrating the sectioning plan used to extract test specimens from the block.

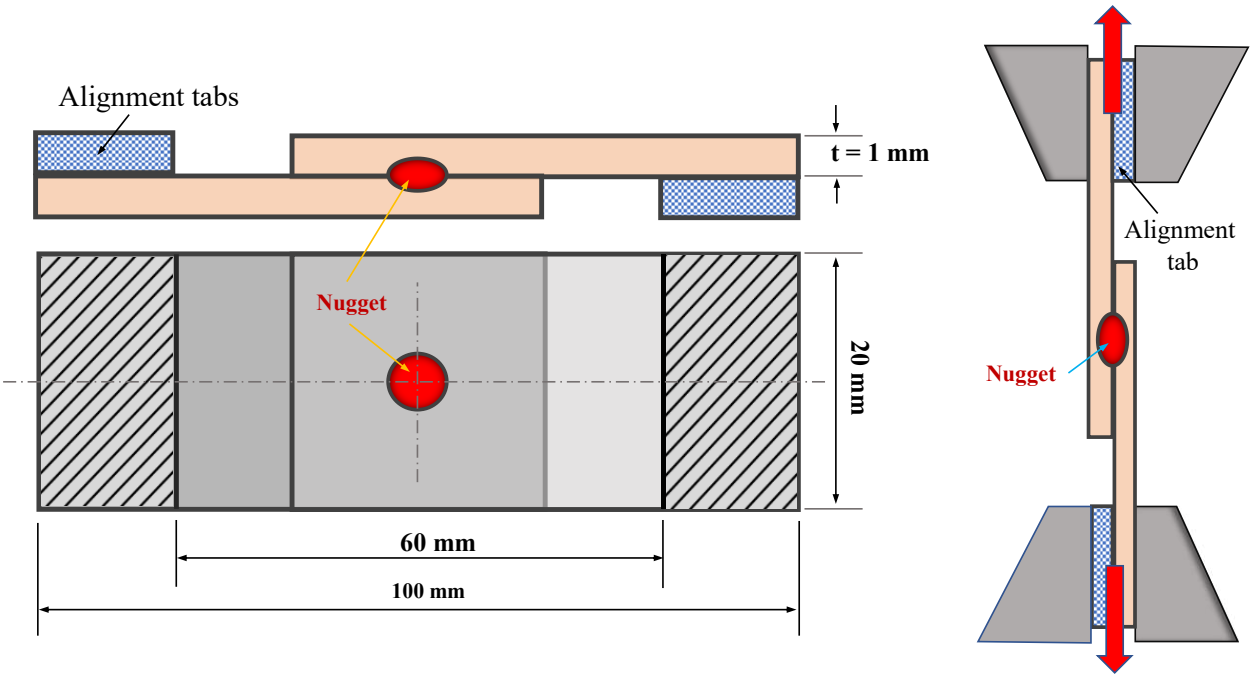



Figure 3. Schematic representation of single-lap resistance spot welded (RSW) specimen geometry and shear-tension test setup.

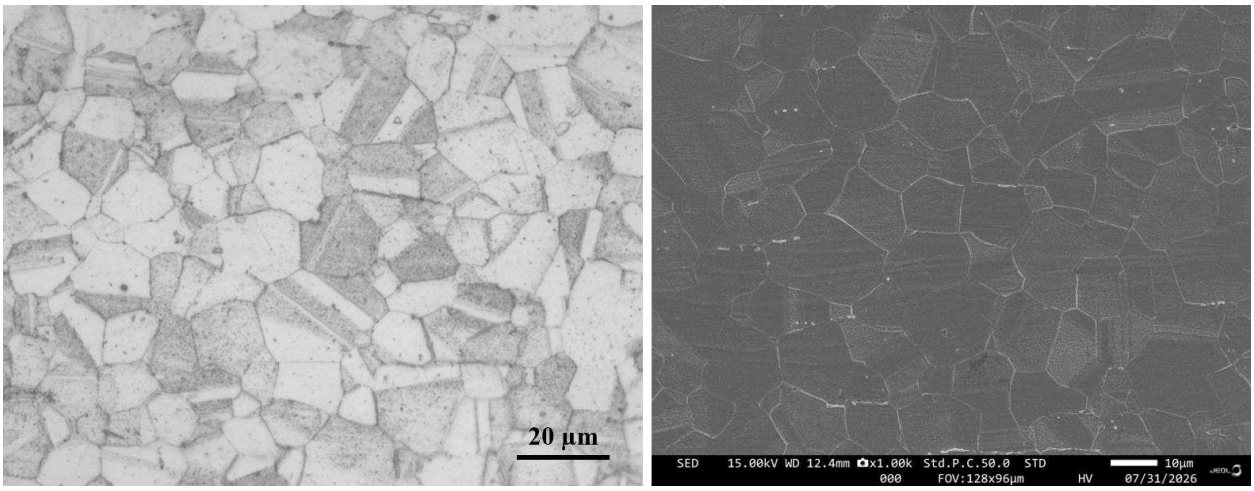



Figure 4. Typical microstructure of the wrought SUS 316L austenite stainless steel using in this study.

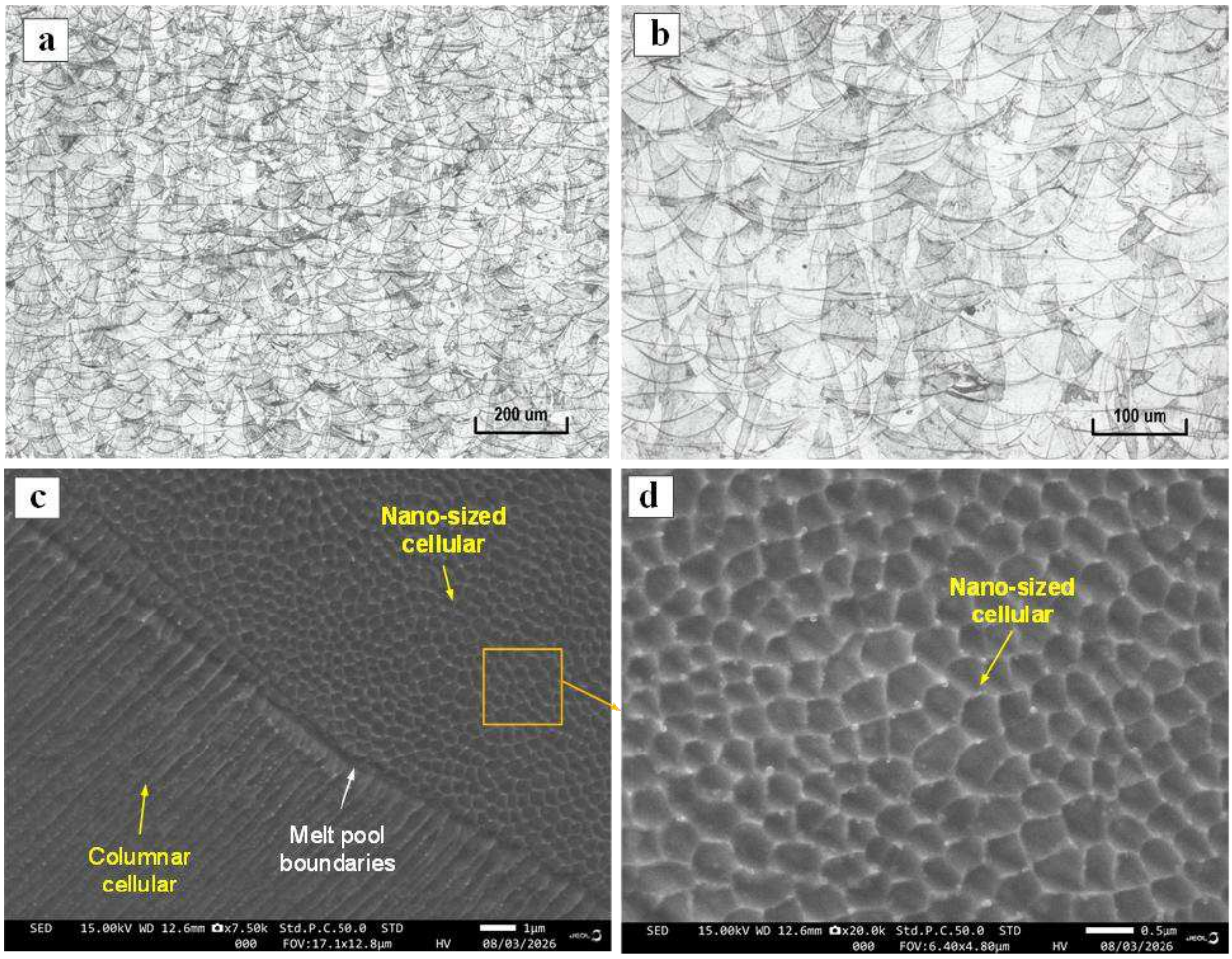



Figure 5. Microstructural characteristics of SLM 316L along the building direction: (a, b) low-magnification micrographs showing overlapping arc-shaped (fish-scale) melt-pool boundaries; (c) SEM image showing the boundary between columnar cellular and nanoscale cellular substructures; and (d) high-magnification SEM image showing the fine cellular network.

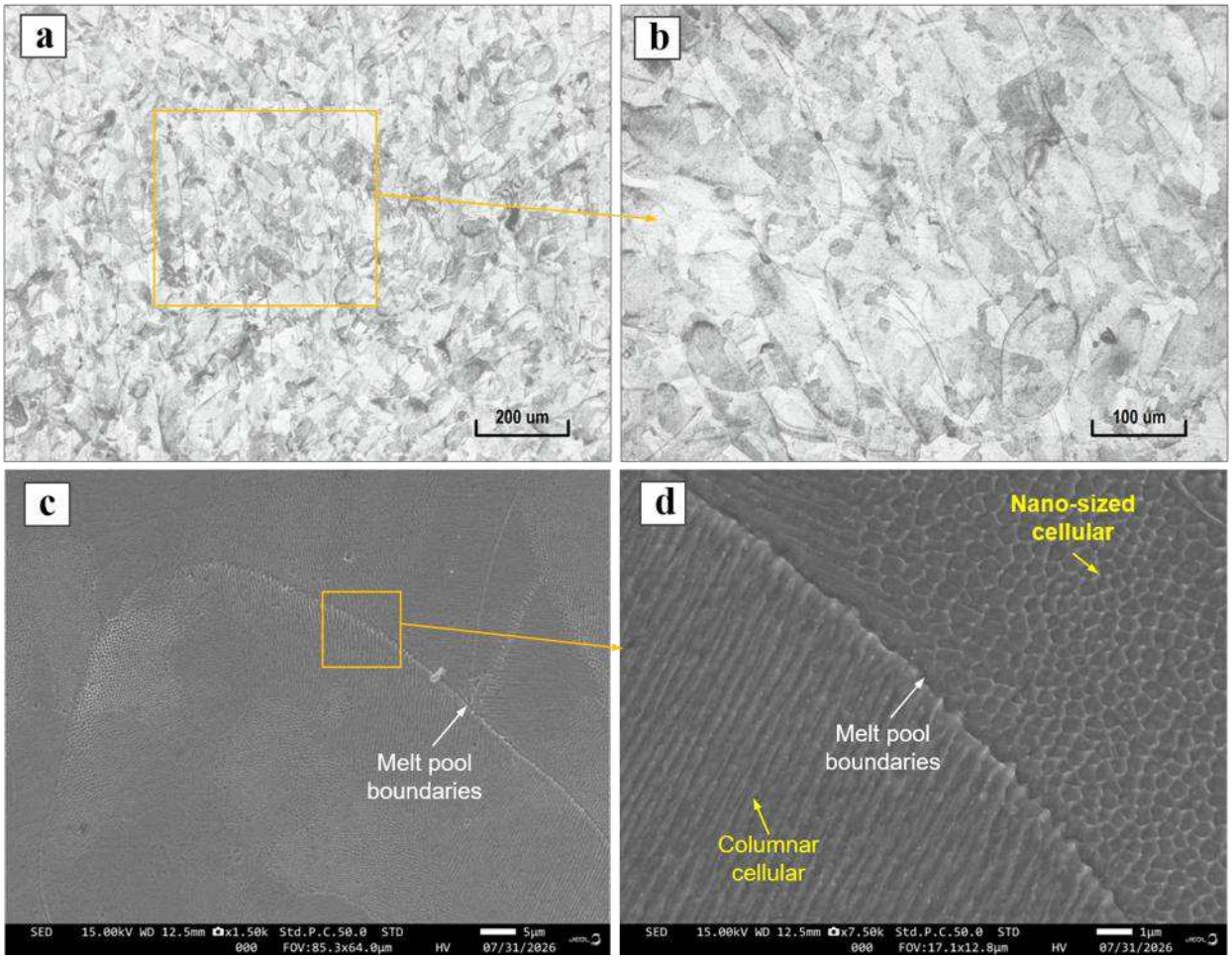



Figure 6. Microstructural characteristics of SLM 316L in the transverse direction: (a, b) low-magnification micrographs showing overlapping laser scan tracks and hatch boundaries; (c) SEM image showing a representative melt-pool boundary with internal subgrain structures; and (d) high-magnification SEM image showing the transition between columnar cellular and nanoscale cellular substructures.

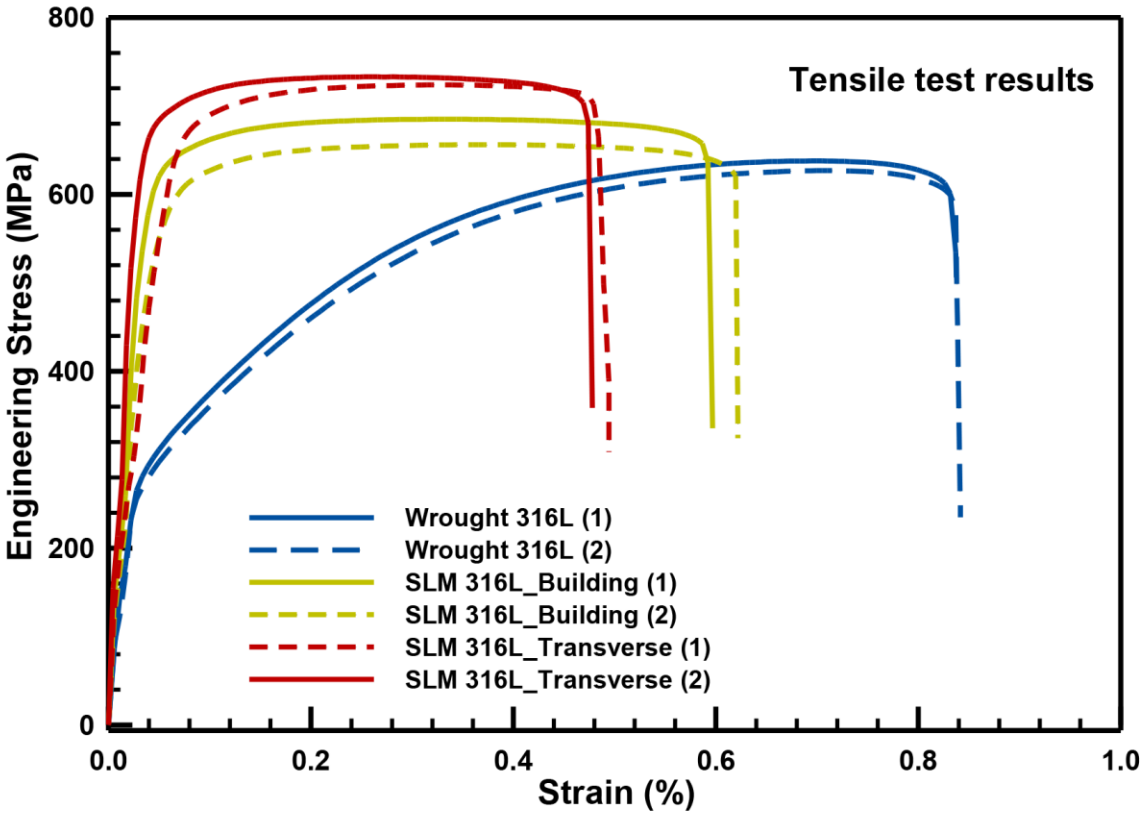



Figure 7. Comparison of engineering stress–strain curves of wrought 316L stainless steel and SLM 316L tested in building and transverse orientations.

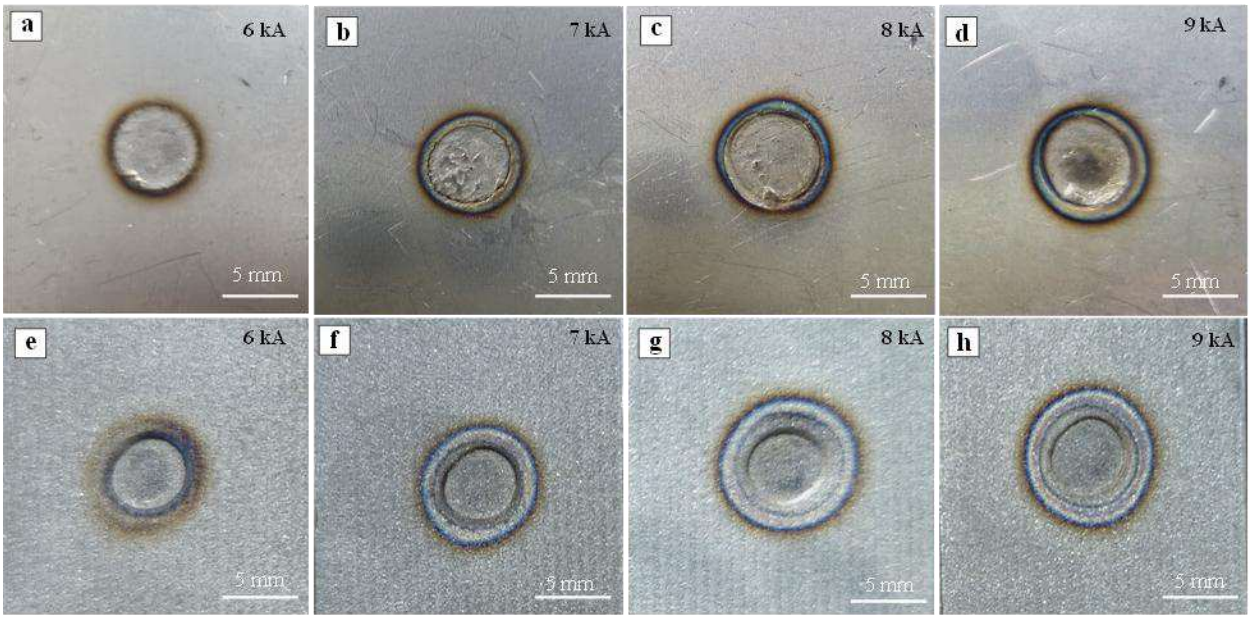



Figure 8. Surface macrographs of RSW joints at welding currents of 6 kA, 7 kA, 8 kA, and 9 kA: (a–d) Wrought 316L sheet surface, and (e–h) SLM 316L (B) sheet surface showing electrode indentation and thermal oxidation ring evolution.

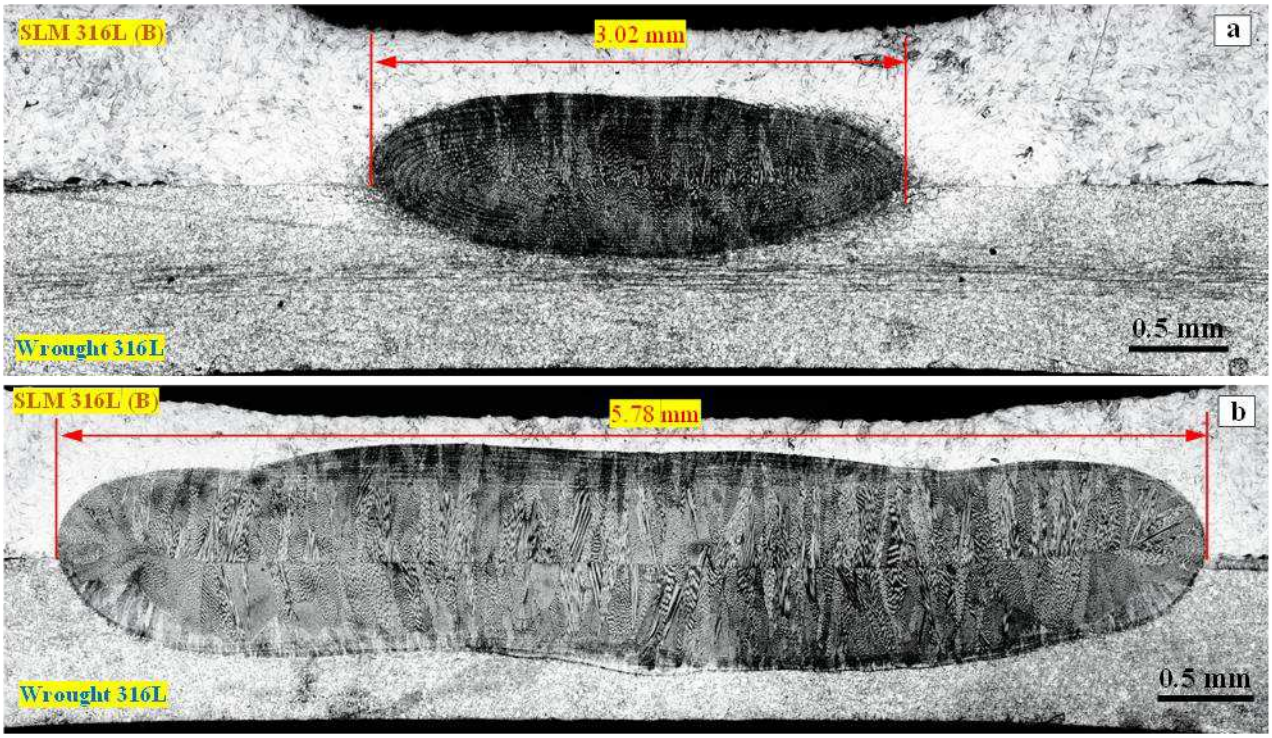



Figure 9. Macrographs showing the nugget geometries of RSW joints between wrought 316L and SLM 316L stainless steels, with the SLM 316L sheet oriented along the building direction: (a) welding current of 6 kA and (b) welding current of 9 kA.

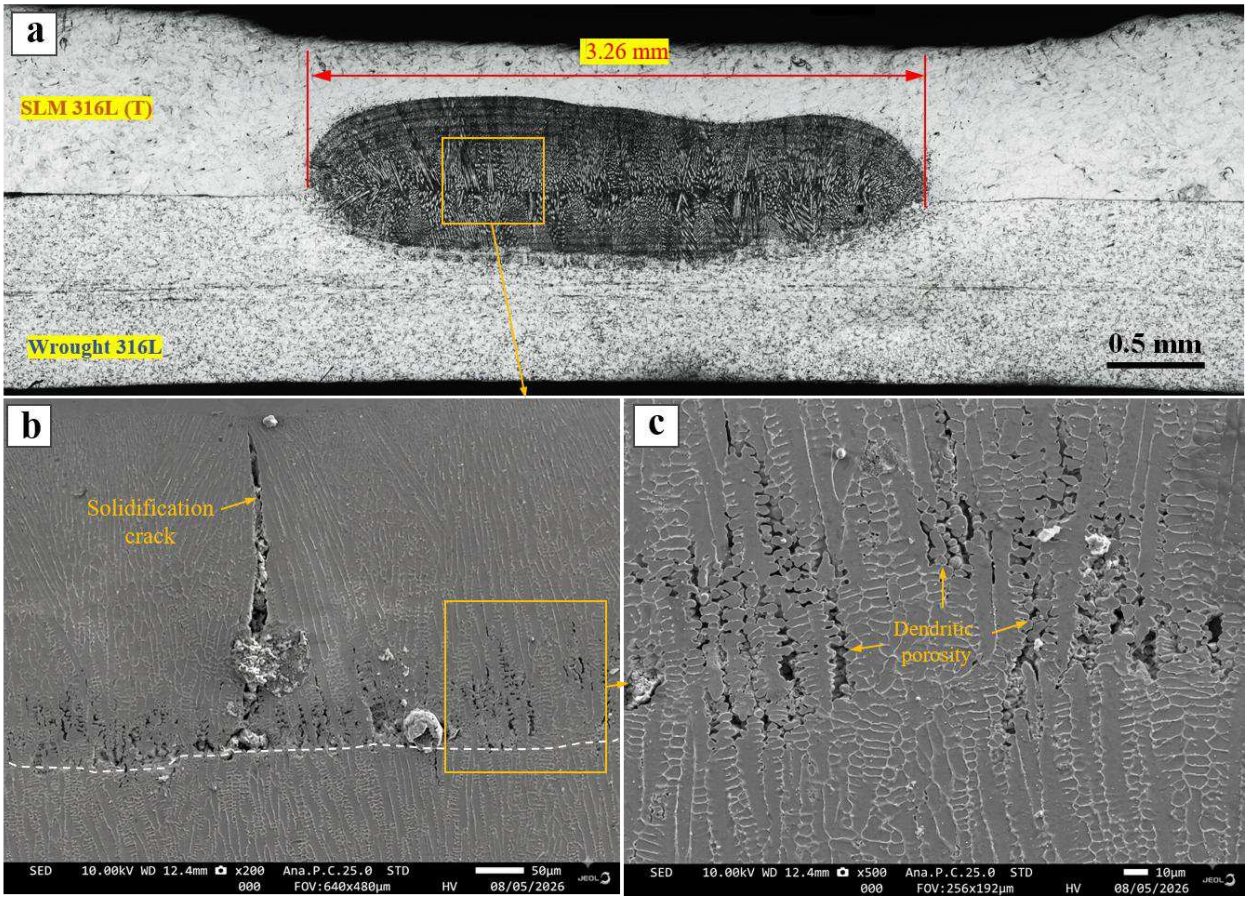



Figure 10. SEM characterization of the resistance spot welded (RSW) joint between SLM 316L (T) and wrought 316L stainless steels. (a) Macroscopic cross-section of the weld nugget and original sheet interface. (b, c) Higher-magnification view showing the dendritic solidification structure, a solidification crack, and the fusion boundary.

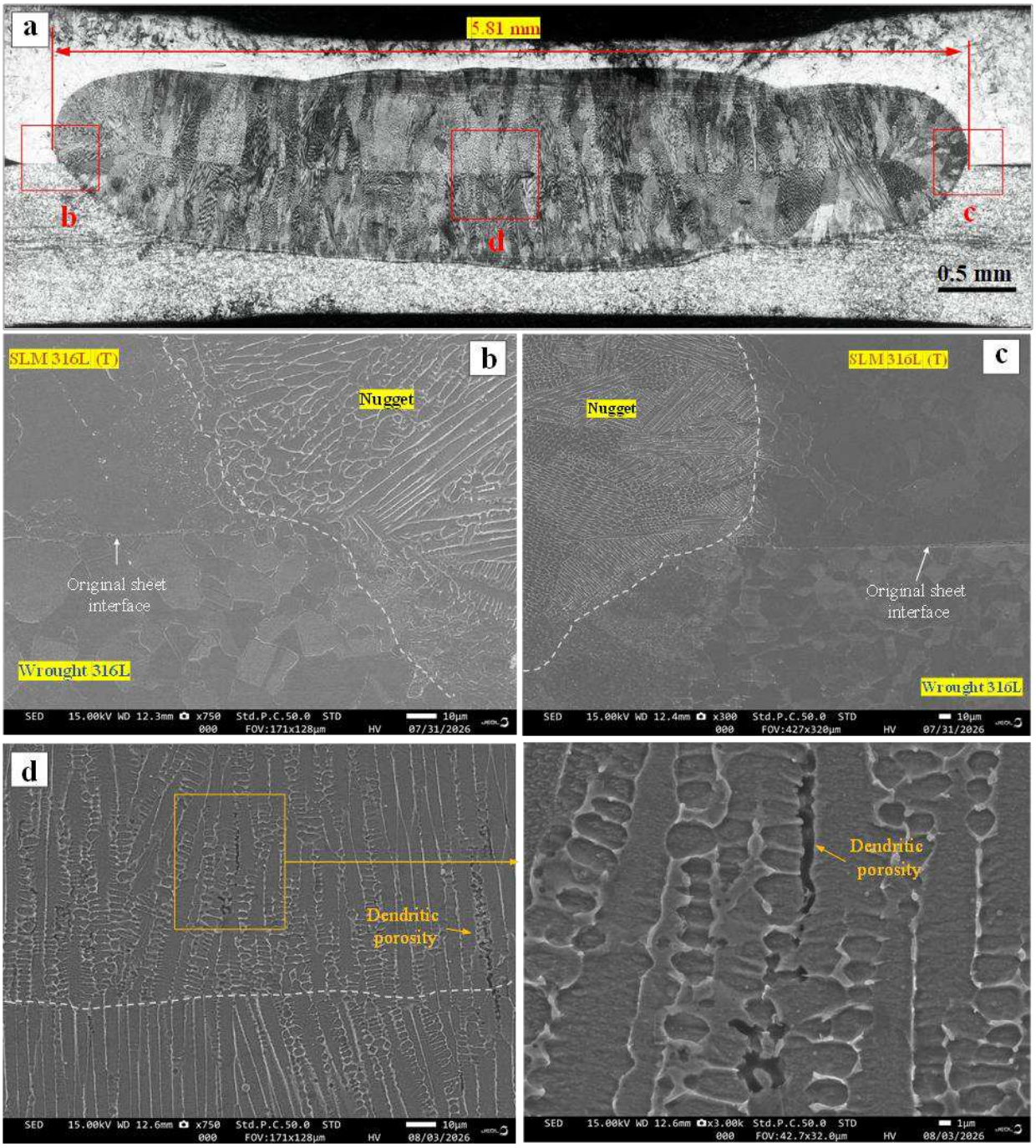
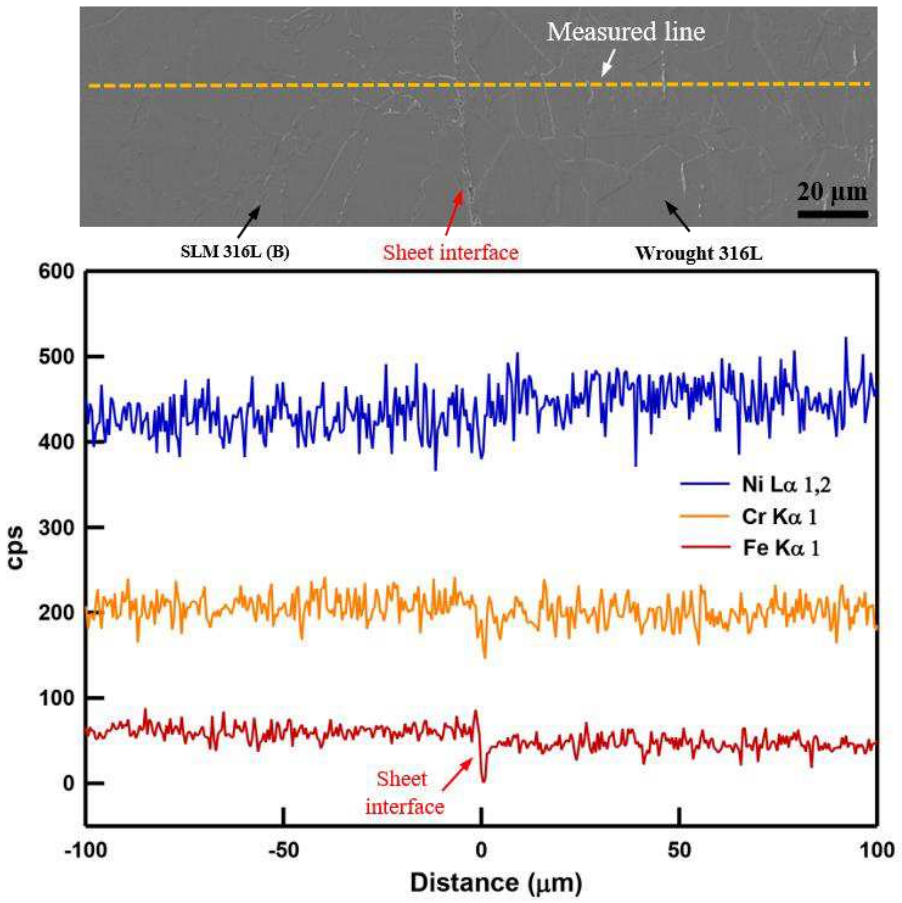



Figure 11. Cross-sectional macrostructure and SEM microstructural features of a dissimilar SLM 316L (T) / Wrought 316L resistance spot weld: (a) full cross-sectional optical micrograph showing a measured weld nugget width of 5.81 mm; (b, c) SEM micrographs of the left and right fusion line boundaries along the original sheet interface; and (d) high-magnification SEM views of the central weld nugget highlighting columnar dendritic solidification and interdendritic porosity.




(a)

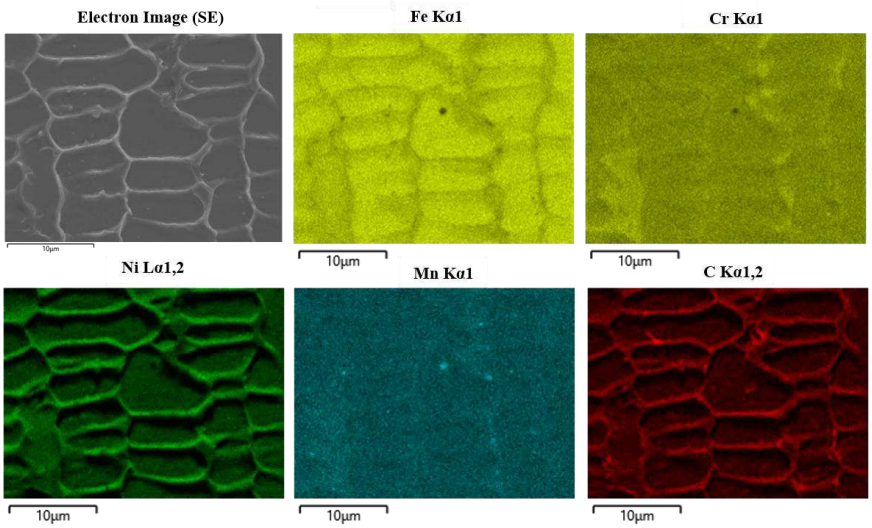
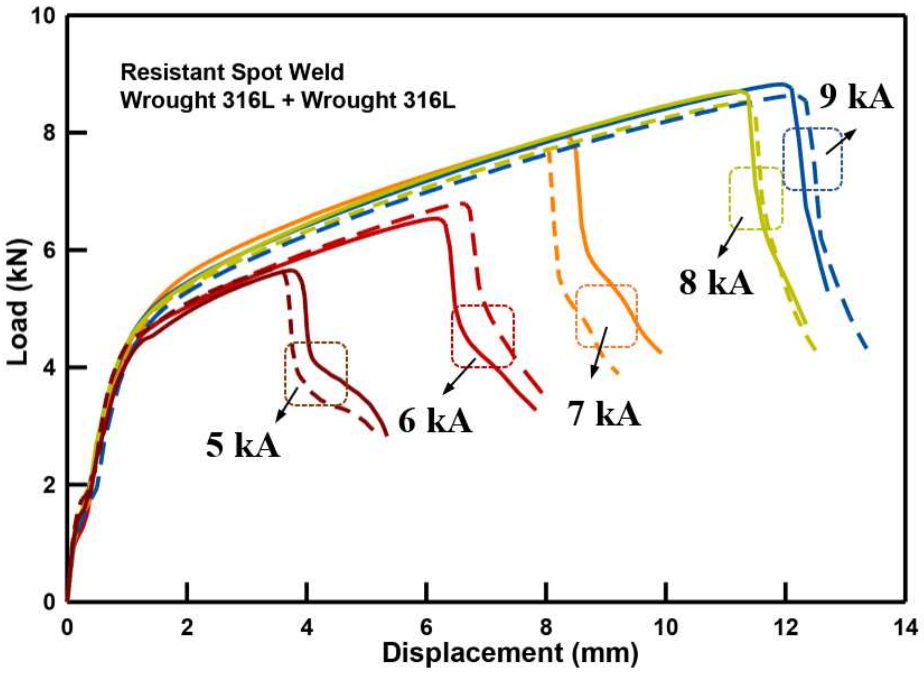
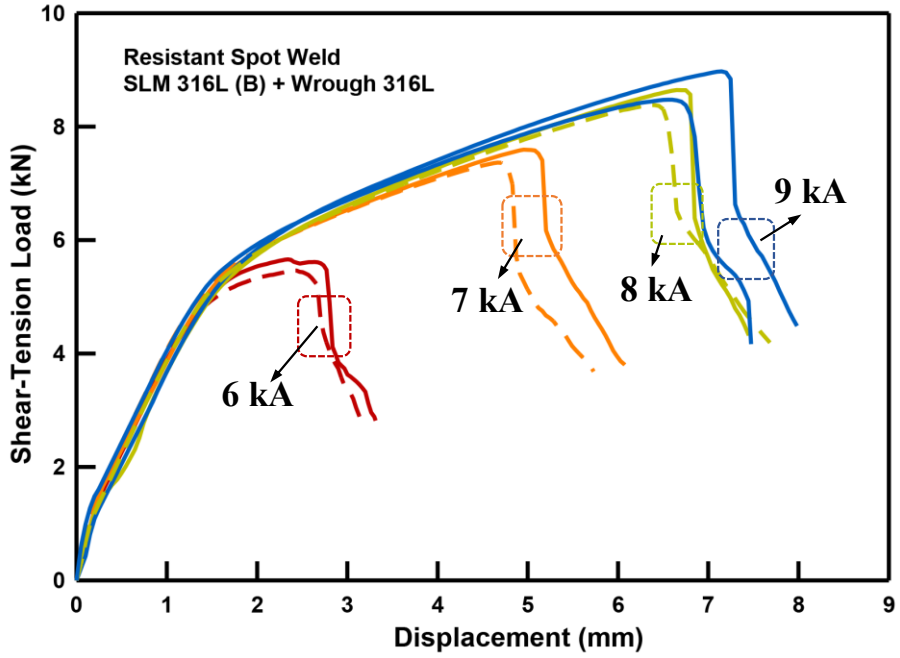


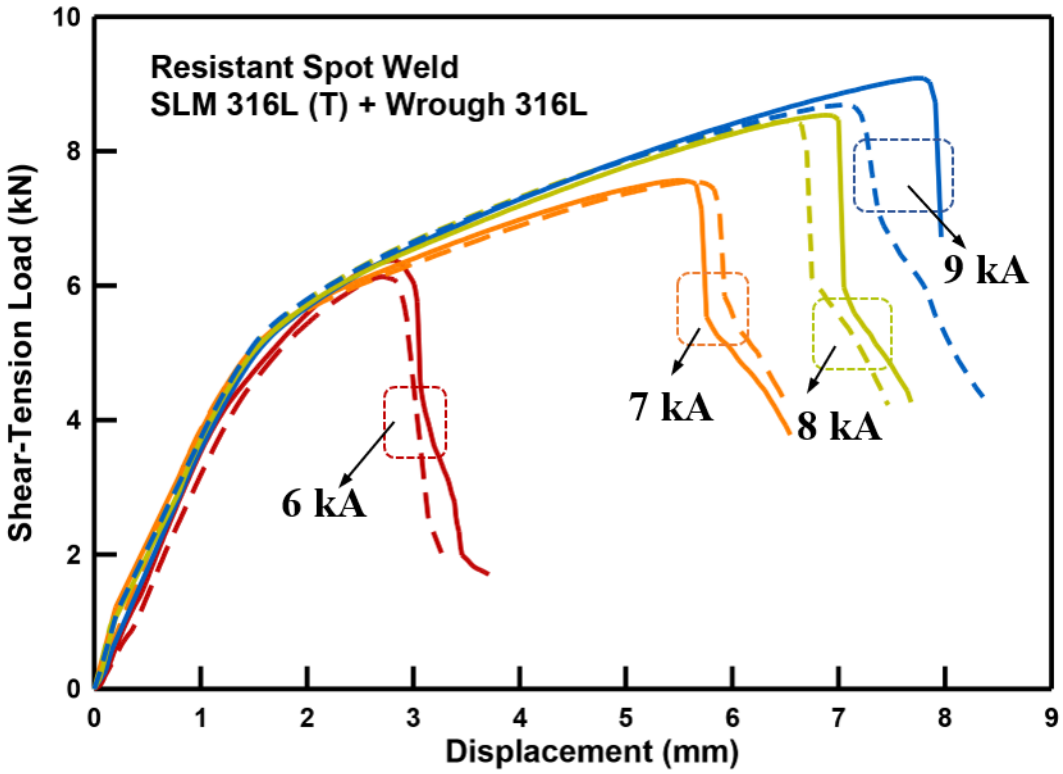

Figure 12. (a) EDS line-scan profiles of Ni, Cr, and Fe across the sheet interface between SLM 316L and wrought 316L in the corona region of the RSW joint (b) EDS elemental maps obtained from the columnar dendritic region on the SLM side of the weld nugget.


Resistant Spot Weld
Wrought 316L + Wrought 316L
Load (kN)
Displacement (mm)
5 kA
6 kA
7 kA
8 kA
9 kA

(a)

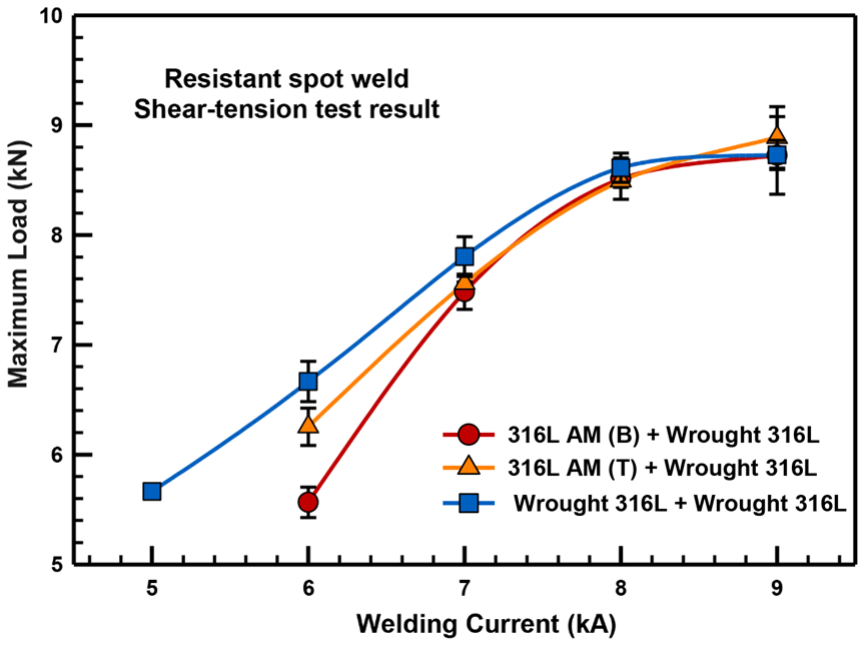

Resistant Spot Weld
SLM 316L (B) + Wrough 316L
Shear-Tension Load (kN)
Displacement (mm)
6 kA
7 kA
8 kA
9 kA

(b)

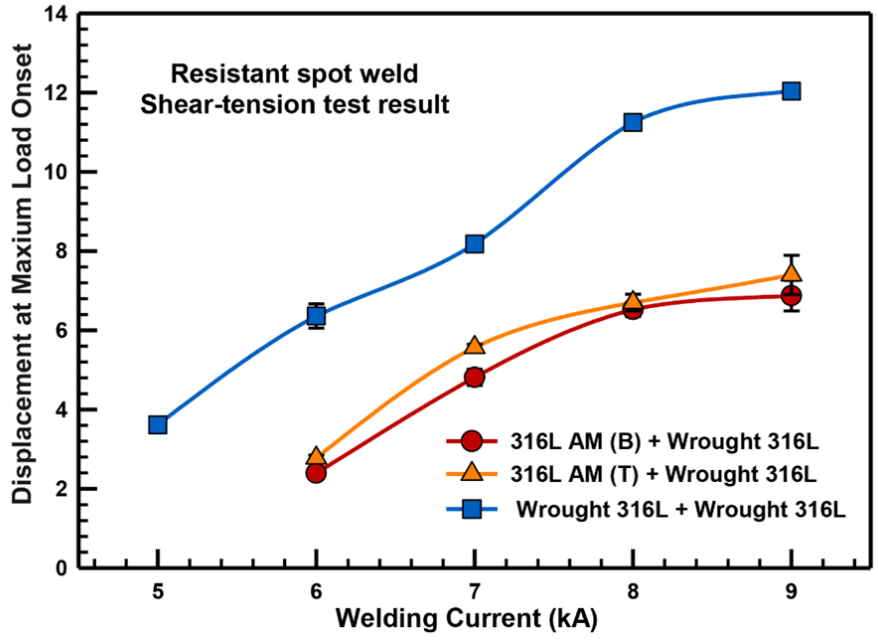



(c)

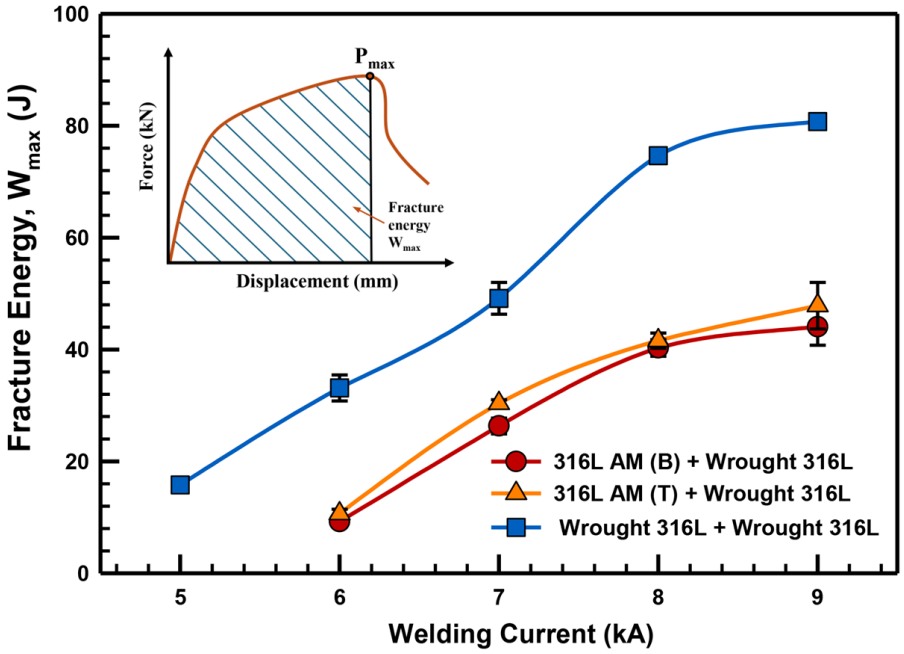
Figure 13. Load–displacement responses of RSW joints between 316L stainless steel sheets at different welding currents: (a) wrought 316L–wrought 316L joints, (b) SLM 316L–wrought 316L joints with the SLM 316L sheet oriented along the building direction, and (c) SLM 316L–wrought 316L joints with the SLM 316L sheet oriented along the transverse direction.


Resistant spot weld
Shear-tension test result
Maximum Load (kN)
Welding Current (kA)
316L AM (B) + Wrought 316L
316L AM (T) + Wrought 316L
Wrought 316L + Wrought 316L

(a)


Resistant spot weld
Shear-tension test result
Displacement at Maxium Load Onset
Welding Current (kA)
316L AM (B) + Wrought 316L
316L AM (T) + Wrought 316L
Wrought 316L + Wrought 316L

(b)




(c)

Figure 14. Comparision of mechanical performance of resistance spot welds under shear-tension testing across welding currents ranging from 5 kA to 9 kA: (a) maximum load carrying capacity, and (b) displacement at maximum load onset, (c) fracture energy.

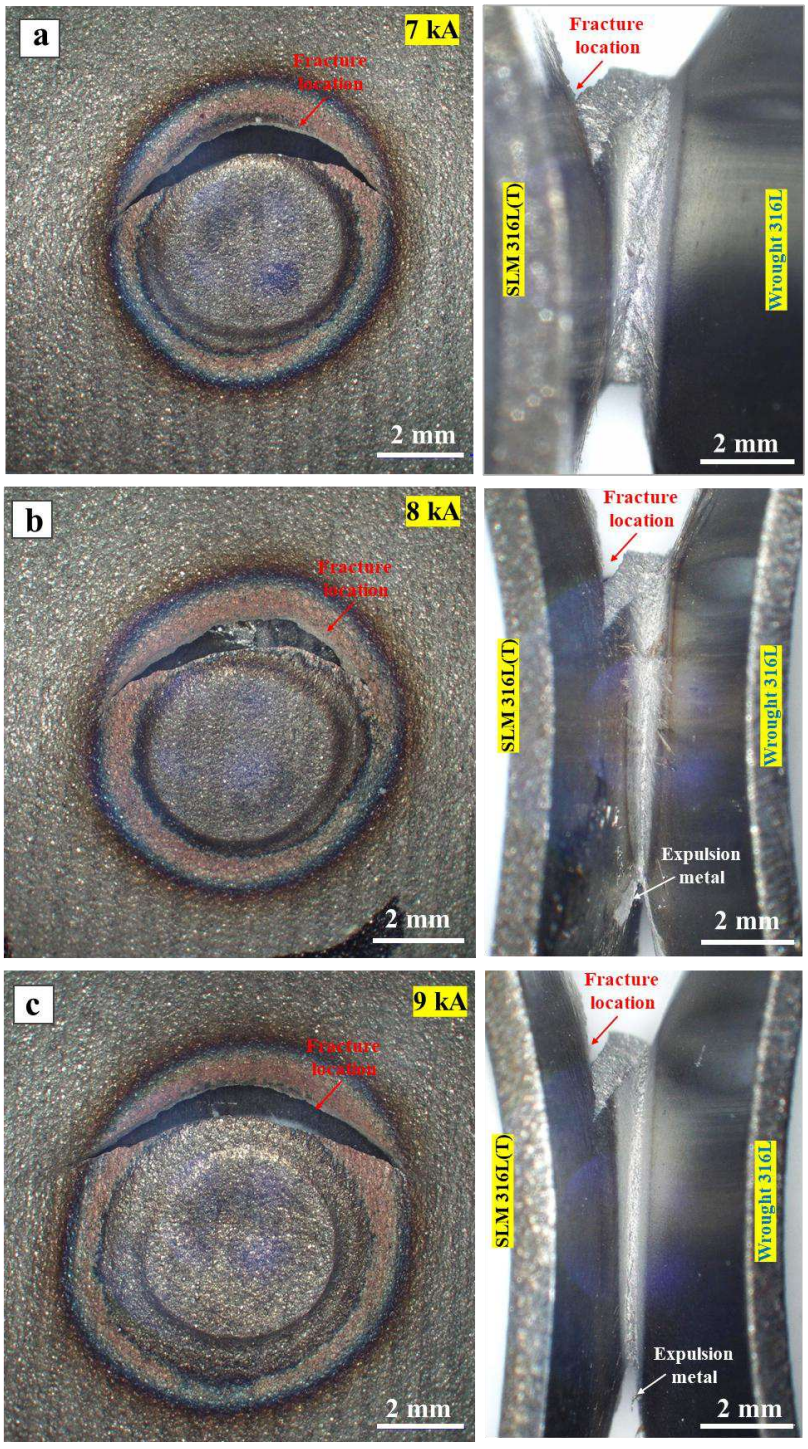



Figure 15. Post-shear-tension macrographs showing failure modes and fracture locations of dissimilar SLM 316L (T)/Wrought 316L resistance spot welds at different welding currents: (a) 7 kA, (b) 8 kA, and (c) 9 kA, detailing the top-down fracture appearance (left) and side-profile view (right).

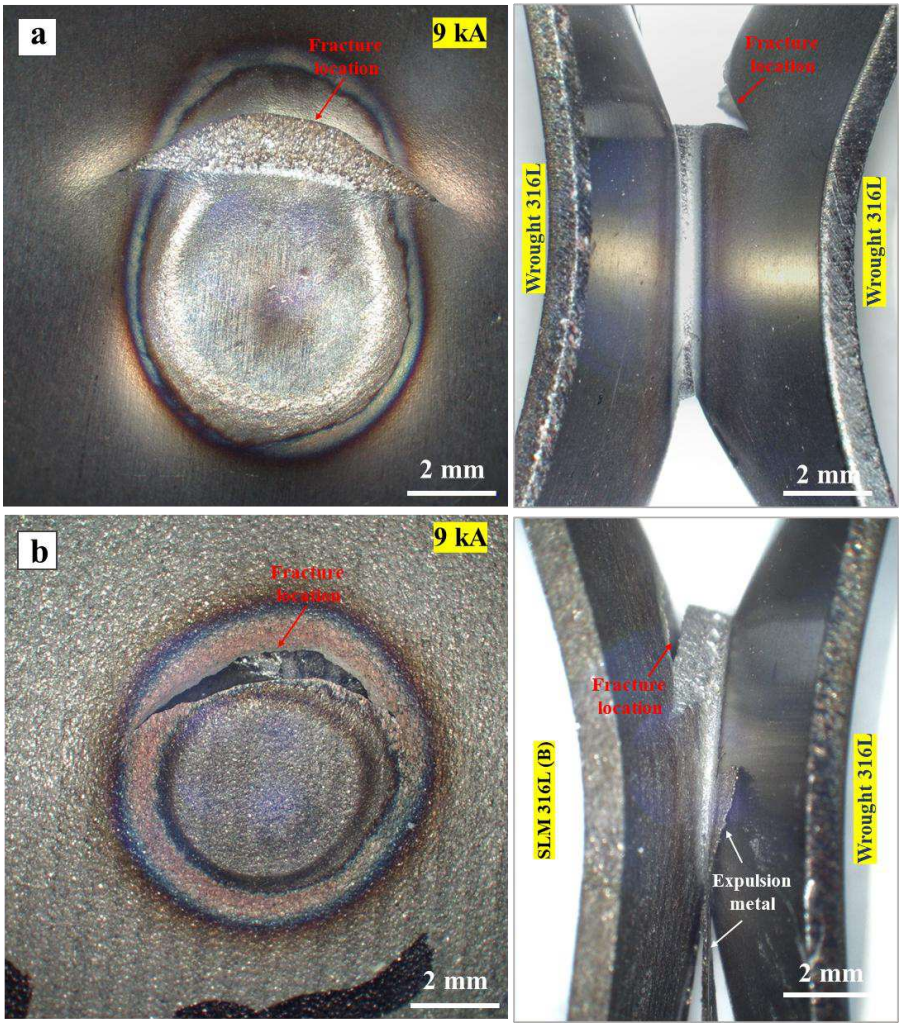



Figure 16. Comparison of post-shear-tension failure modes and fracture locations for resistance spot welds produced at 9 kA: (a) similar Wrought 316L/Wrought 316L joint, and (b) dissimilar SLM 316L (B)/Wrought 316L joint, showing top-down fracture appearance (left) and side-profile view (right).

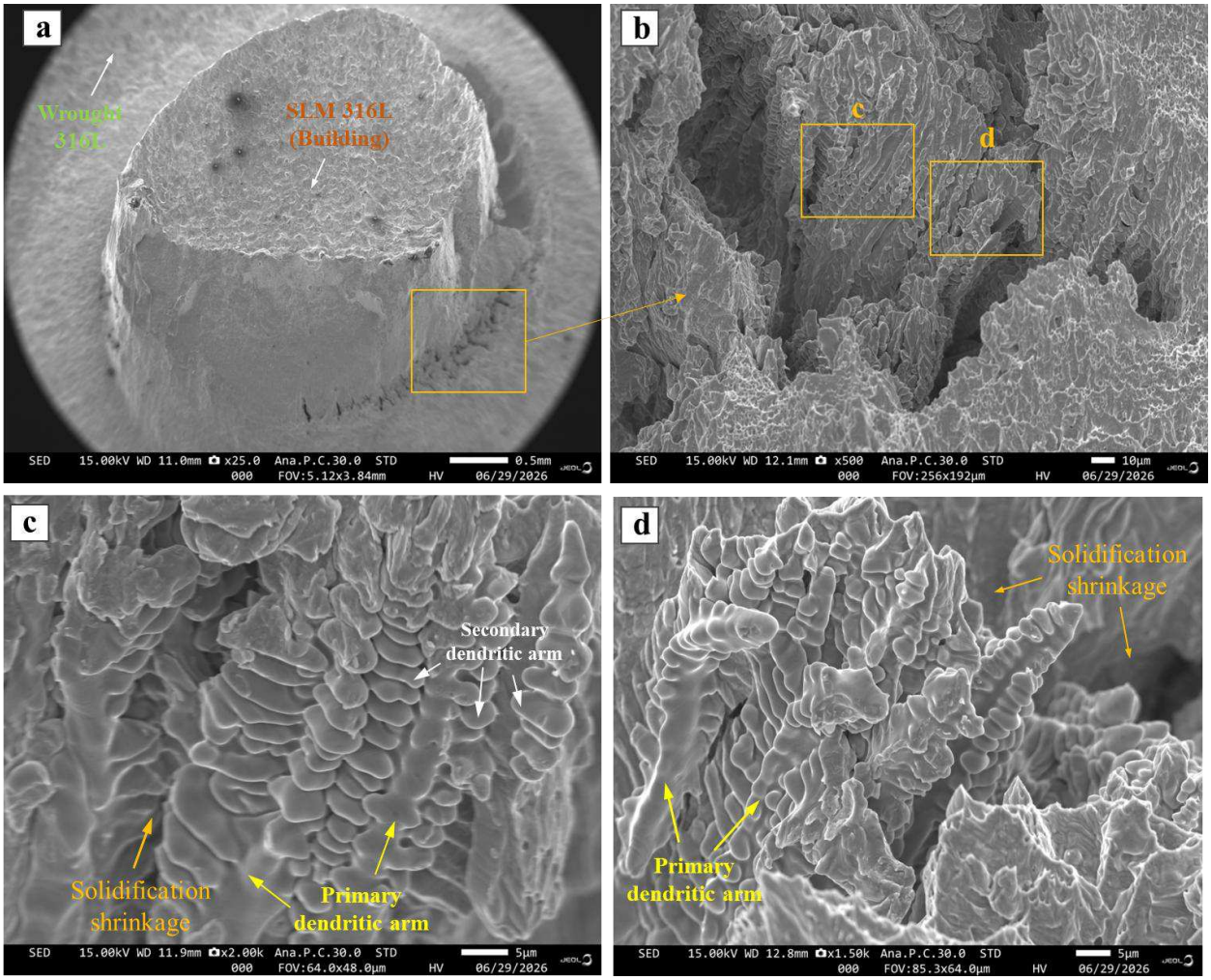



Figure 17. Fracture surface morphology of the resistance spot weld at a welding current of 6 kA after the tensile-shear test, exhibiting a pull-out fracture mode: (a) macroscopic overview of the pulled-out weld button showing the Wrought 316L and SLM 316L regions; (b) microfracture morphology near the periphery of the fracture region; (c), (d) detailed morphology adjacent to the tearing edge, highlighting primary and secondary dendritic arms alongside solidification shrinkage.